UNIVERSITAT POLITÈCNICA DE VALÈNCIA

Study of Feasible Cell-Free Massive MIMO Systems in Realistic Indoor Scenarios

Departamento de Comunicaciones
Universitat Politècnica de València

A thesis submitted for the degree of
Doctor por la Universitat Politècnica de València
Valencia, December 2022

Author:
Danaisy Prado Alvarez

Supervisors:
Dr. Jose F. Monserrat del Río
Dr. David Martín-Sacristán Gandía

Debes amar el tiempo de los intentos;
debes amar la hora que nunca brilla;
y si no, no pretendas tocar lo cierto ...
J.M.

Abstract

The massive use of telecommunications demands higher capacity networks. This capacity can be increased by increasing the number of antennas, bandwidth, spectral efficiency, or a combination of these. In response to this, cell-free massive Multiple-Input Multiple-Output (MIMO) systems have emerged. These systems aim to offer a ubiquitous and reliable service, relying on a massive number of antennas and adapting the network to users' needs. Cell-free massive MIMO systems have been studied both for frequencies below 6 GHz and in the millimeter Wave (mmW) band, proving to be a good alternative to small cells. However, many issues still require further study. This Thesis addresses the issues concerning cell-free massive MIMO deployments in terms of scalability, power consumption, realistic modeling of deployment scenarios, and design of precoders for such scenarios in the mmW band.

Cell-free massive systems in their canonical form consider that all the Access Points (APs) are connected to a single Central Processing Unit (CPU) and serve all User Equipments (UEs) simultaneously. However, in practice, such a system is not feasible, due to scalability reasons. Therefore, in this Thesis, different clustering solutions that alleviate the load of both each individual AP and the CPUs, as the total processing load is divided among them, are studied and proposed. The proposed solutions show a better performance than the state-of-the-art solution studied for all cluster sizes considered and independently of the number of UEs in the scenario.

After the logical network topology considerations, the impact on the network performance of different physical topologies configurations is analyzed. Specifically, the power consumption modeling considering fully dedicated, hybrid, and fully serial front-haul is studied. In this sense, some modifications are suggested for the traditional power consumption model in order to get more accurate results when serial environments are analyzed. The obtained results highlight the importance of applying the proposed modifications that consider the power savings due to the serial connections in a cell-free massive MIMO deployment where each AP transmits the same information (except by the precoding coefficients).

On the other hand, although wider bandwidths are available in the millimeter band, the use of these frequencies brings certain challenges. One of these challenges is modeling the radio channel since when working with wavelengths in the order of tens of millimeters, any object or roughness of the same order can affect the propagation of the wave. Another challenge is to consider the electro-

magnetic impact of the human body at mmW frequencies. In this sense, this Thesis, firstly, proposes some adaptations to the Third Generation Partnership Project (3GPP) body blockage model. The results obtained after the modifications are closer to real measurement values, what makes the adapted model more accurate for the consideration of body blockage at mmW. Secondly, this Thesis presents a radio channel simulation tool based on ray tracing. With this tool, pathloss results have been obtained for an indoor scenario that are remarkably close to the actual measurements. Also, the results show that when the electromagnetic characteristics of the materials are not modeled correctly or the furniture is not taken into account in an indoor scenario, the adjustment of the simulation results can differ considerably from the real measurements.

Finally, the design of precoders in cell-free massive MIMO systems in a realistic scenario is addressed. For this purpose, an industrial scenario with specific power requirements is considered. In particular, an optimization problem with different per-antenna power constraints is solved. In this case, the scenario and the radio channel are modeled using the above mentioned tool. This fact makes it possible to find with high precision the power coefficients to be used by each transmitting antenna to transmit to each user so that the achieved data rate is maximized.

Resumen

El uso masivo de las telecomunicaciones exige redes de mayor capacidad. Esta capacidad puede incrementarse de las siguientes maneras: aumentando el número de antenas, aumentando el ancho de banda, aumentando la eficiencia espectral o una combinación de ellas. En respuesta a esto, han surgido los sistemas masivos MIMO sin celdas. Estos sistemas pretenden ofrecer un servicio ubicuo y fiable, apoyándose en un número masivo de antenas y adaptando la red a las necesidades de los usuarios en cada momento. Se han estudiado sistemas MIMO masivos sin celdas tanto para frecuencias inferiores a 6 GHz como en la banda mmW, demostrando ser una buena alternativa a las celdas pequeñas. Sin embargo, hay muchas cuestiones que todavía requieren más estudio. Esta Tesis aborda las cuestiones relativas a los despliegues masivos MIMO sin celdas en términos de escalabilidad, consumo de energía, modelado realista de los escenarios de despliegue y diseño de precodificadores para dichos escenarios en la banda mmW.

Los sistemas masivos sin celdas en su forma canónica consideran que todos los APs están conectados a una única CPU y que todos ellos sirven a todos los UEs al mismo tiempo. Sin embargo, en la práctica, tal sistema no es factible debido a temas de escalabilidad. Por ello, en esta Tesis se estudian y proponen diferentes soluciones de agrupación que alivian la carga tanto de cada AP individual como de las CPUs, ya que la carga total de procesamiento se divide entre ellas. Las soluciones propuestas muestran un mejor rendimiento que la solución del estado del arte estudiada para todos los tamaños de agrupación considerados e independientemente del número de UEs en el escenario.

Tras las consideraciones sobre la topología lógica de la red, esta Tesis analiza el impacto en el rendimiento de la red de diferentes configuraciones de topologías físicas. En concreto, se estudia el modelado del consumo de energía considerando front-haul totalmente dedicado, híbrido y totalmente en serie. En este sentido, se sugieren algunas modificaciones al modelo tradicional de consumo de energía para obtener resultados más precisos cuando se analizan entornos en serie. A partir de los resultados obtenidos, se destaca la importancia de aplicar las modificaciones propuestas que consideran el ahorro de energía debido a las conexiones serie en un despliegue de MIMO masivo sin celdas donde cada AP transmite la misma información (excepto por los coeficientes de precodificación).

Por otro lado, aunque en la banda milimétrica se dispone de mayores anchos de banda, el uso de estas frecuencias conlleva ciertos retos. Uno de estos retos

es el modelado del canal radioeléctrico, ya que al trabajar con longitudes de onda del orden de decenas de milímetros cualquier objeto o rugosidad del mismo puede afectar a la propagación de la onda. En este sentido, esta Tesis, en primer lugar, propone algunas adaptaciones al modelo de bloqueo del cuerpo humano del 3GPP. Los resultados obtenidos tras las modificaciones se acercan más a los valores de las mediciones reales, lo que hace que el modelo adaptado sea más preciso para la consideración del bloqueo corporal en mmW. En segundo lugar, esta Tesis presenta una herramienta de simulación de radiocanales basada en el trazado de rayos. Con esta herramienta, se han obtenido resultados de pérdidas de trayecto para un escenario de interior que se aproximan notablemente a las medidas reales. Asimismo, los resultados obtenidos muestran que cuando no se modelan correctamente las características electromagnéticas de los materiales o no se tiene en cuenta el mobiliario en un escenario de interior, el ajuste de los resultados de la simulación puede diferir considerablemente de las medidas reales.

Por último, esta Tesis aborda el diseño de precodificadores en sistemas MIMO masivos sin celdas en un escenario realista. Para ello, se considera un escenario industrial con requerimientos de potencia específicos. En particular, se resuelve un problema de optimización con diferentes restricciones de potencia por antena. En este caso, tanto el escenario como el canal radioeléctrico se modelan con la herramienta mencionada anteriormente. Este hecho permite encontrar con gran precisión los coeficientes de potencia que debe utilizar cada antena transmisora para transmitir a cada usuario de forma que se maximice la tasa de datos alcanzada.

Resum

L'ús massiu de les telecomunicacions exigeix xarxes de major capacitat. Aquesta capacitat pot incrementar-se de les següents maneres: augmentant el nombre d'antenes, augmentant l'amplada de banda, augmentant l'eficiència espectral o una combinació d'elles. En resposta a això, han sorgit els sistemes massius MIMO sense cel·les. Aquests sistemes pretenen oferir un servei ubic i fiable, secundant-se en un nombre massiu d'antenes i adaptant la xarxa a les necessitats dels usuaris a cada moment. S'han estudiat sistemes MIMO massius sense cel·les tant per a freqüències inferiors a 6 GHz com en la banda mmW, que han demostrat ser una bona alternativa a les cel·les xicotetes. No obstant això, hi ha moltes qüestions que encara requereixen més estudi. Aquesta Tesi aborda les qüestions relatives als desplegaments massius MIMO sense cel·les en termes d'escalabilitat, consum d'energia, modelatge realista dels escenaris de desplegament i disseny de precodificadors per a aquests escenaris en la banda mmW.

Els sistemes massius sense cel·les en la seua forma canònica consideren que tots els APs estan connectats a una única CPU i que tots ells serveixen a tots els UEs al mateix temps. No obstant això, en la pràctica, tal sistema no és factible a causa de temes d'escalabilitat. Per això, en aquesta Tesi s'estudien i proposen diferents solucions d'agrupació que alleugen la càrrega tant de cada AP individual com de les CPUs, ja que la càrrega total de processament es divideix entre elles. Les solucions proposades mostren un millor rendiment que la solució de l'estat de l'art estudiada per a totes les grandàries d'agrupació considerades i independentment del nombre de UEs en l'escenari.

Després de les consideracions sobre la topologia lògica de la xarxa, aquesta Tesi analitza l'impacte en el rendiment de la xarxa de diferents configuracions de topologies físiques. En concret, s'estudia el modelatge del consum d'energia considerant un front-haul totalment dedicat, híbrid i totalment en sèrie. En aquest sentit, se suggereixen algunes modificacions al model tradicional de consum d'energia per a obtindre resultats més precisos quan s'analitzen entorns en sèrie. A partir dels resultats obtinguts, es destaca la importància d'aplicar les modificacions proposades que consideren l'estalvi d'energia a causa de les connexions sèrie en un desplegament de MIMO massiu sense cel·les on cada AP transmet la mateixa informació (excepte pels coeficients de precodificació).

D'altra banda, encara que a la banda mil·limètrica es disposa de majors amplades de banda, l'ús d'aquestes freqüències comporta uns certs reptes. Un d'aquests reptes és el modelatge del canal radioelèctric, ja que en treballar

amb longituds d'ona de l'ordre de desenes de mil·límetres qualsevol objecte o rugositat del mateix pot afectar la propagació de l'ona. En aquest sentit, aquesta Tesi, en primer lloc, proposa algunes adaptacions al model de bloqueig del cos humà del 3GPP. Els resultats obtinguts després de les modificacions s'acosten més als valors dels mesuraments reals, la qual cosa fa que el model adaptat siga més precís per a la consideració del bloqueig corporal en mmW. En segon lloc, aquesta Tesi presenta una eina de simulació de radiocanals basada en el traçat de raigs. Amb aquesta eina, s'han obtingut resultats de pèrdues de trajecte per a un escenari d'interior que s'aproximen notablement a les mesures reals. Així mateix, els resultats obtinguts mostren que quan no es modelen correctament les característiques electromagnètiques dels materials o no es té en compte el mobiliari en un escenari d'interior, l'ajust dels resultats de la simulació pot diferir considerablement de les mesures reals.

Finalment, aquesta Tesi aborda el disseny de precodificadors en sistemes MIMO massius sense cel·les en un escenari realista. Per a això, es considera un escenari industrial amb requeriments de potència específics. En particular, es resol un problema d'optimització amb diferents restriccions de potència per antena. En aquest cas, tant l'escenari com el canal radioelèctric es modelen amb l'eina esmentada anteriorment. Aquest fet permet trobar amb gran precisió els coeficients de potència que ha d'utilitzar cada antena transmissora per a transmetre a cada usuari de manera que es maximitze la taxa de dades aconseguida.

Acknowledgements

First, I would like to thank the H2020 Marie Curie Program that has funded this Thesis within Project Grant No. 766231 WAVECOMBE - ITN - 2017. Thank you for the opportunity to be able to focus entirely on research.

Taking a doctorate is undoubtedly a challenging road to travel. I feel very fortunate to have had the support to get this far. I would like to thank my supervisors. I thank Prof. Jose F. Monserrat for his help, his availability at any time, and for always seeing me as a doctor-to-be. Special thanks to Dr. David Martín-Sacristán for getting me out of all the technical and emotional jams.

I would also like to thank all the members of the WaveComBE project, especially my colleagues Mohammad and Monika, who made my stays in the UK and Belgium memorable. Thanks to the MCG family (I prefer not to mention names) for making our office the best shelter.

Thanks to Prof. Eduard Jorswieck, Prof. Ana García Armada, and Dr. Xavier Gelabert Doran for their work as reviewers of this Thesis. Thanks to Prof. Ana García Armada, Prof. Narcís Cardona, and Dr. Paolo Grazioso for serving as committee members.

Finally, I would like to thank my family for their unconditional love and support, even paying the price of distance; my everlasting friends; and, of course, my Love.

Danaisy Prado Alvarez

Table of contents

List of Figures

List of Tables

Acronyms

1G	First Generation
3D	Three Dimensions
3GPP	Third Generation Partnership Project
4G	Fourth Generation
5G	Fifth Generation
AP	Access Point
AWGN	Additive White Gaussian Noise
BS	Base Station
BB	Base Band
BC	Broadcast
CDF	Cumulative Distribution Function
CPU	Central Processing Unit
CSI	Channel State Information
D2D	Device-to-Device
DL	Downlink
DKED	Double Knife-Edge Diffraction
DPC	Dirty Paper Coding
eMBB	Enhanced Mobile Broadband
EHF	Extremely High Frequency
EV	Exclusion Volume
GI	Global Illumination
IMT	International Mobile Telecommunications
IMT-2020	IMT 2020

IMT-Advanced	IMT Advanced
LIM	Light Intensity Model
LoS	Line of Sight
METIS	Mobile and wireless communications Enablers for Twenty-twenty Information Society
MIMO	Multiple-Input Multiple-Output
mMTC	massive Machine Type Communications
mmW	millimeter Wave
MRT	Maximum Ratio Transmission
MMF	Max-Min Fairness
MAC	Multiple Access Channel
MF	Matched Filtering
NLoS	Non Line of Sight
QoS	Quality of Service
RT	Ray Tracing
RX	Receiver
RF	Radio Frequency
SINR	Signal to Interference plus Noise Ratio
SHF	Super High Frequency
SE	Spectral Efficiency
SC	Small Cell
SIC	Successive Interference Cancellation
TDD	Time Division Duplexing
TX	Transmitter
UE	User Equipment
UL	Uplink
URLLC	Ultra-Reliable and Low Latency Communications
VNA	Vector Network Analyzer
ZF	Zero Forcing

Notation

This section describes the notation used in this Thesis.

$\mathbf{A}$ (boldface capital letter) and $\mathbf{A}_k$ represent matrices.
$\mathbf{A}^H$ denotes the conjugate transpose or Hermitian transpose of $\mathbf{A}$.
$\mathbf{a}$ (boldface lower-case letter) and $\mathbf{a}_k$ represent vectors.
a and A (not boldface italic letters) represent scalars.
$\mathcal{A}$ Set.
$\mathbb{C}$ Complex numbers.
$|\mathcal{A}|$ Cardinality of $\mathcal{A}$.
$\mathbb{E}[X]$ Expected value of X.
$\mathcal{CN}(\mu, \sigma^2)$ Circulary-symetric complex Gaussian distribution with mean μ and variance σ^2.

Chapter 1

Introduction

This Thesis presents the results of a research activity focused on the field of cell-free massive Multiple-Input Multiple-Output (MIMO) systems. Specifically, the thesis addresses scalability, power consumption, realistic channel modeling for millimeter Wave (mmW), and signal processing in cell-free massive MIMO systems. This introductory chapter describes the framework of the Thesis and provides the elemental background to follow the scientific discussion. Moreover, the motivation of the research is exposed, leaving the problems to be solved in light.

For the sake of deepening, this chapter has been split into the following sections:

- Section 1.1 presents the technological frame of the Thesis. The main concepts related to analyzing mmW communications in indoor environments are introduced.
- Section 1.2 describes the state of the art of topics that fall within the scope of this Thesis.
- Section 1.3 identifies the problems to be tackled.
- Section 1.4 enunciates the hypothesis and objectives of the Thesis.
- Section 1.5 outlines the structure of the Thesis, giving a brief overview of each chapter.
- Section 1.6 lists the publications related to this Thesis, including journal and conference papers.

1.1 Background

Former mobile generations (from First Generation (1G) to Fourth Generation (4G)) had in common that all of them intended to give a wider range of services (voice calls, short messages, internet connection, etc.) at a better quality to the same final user: humans. Although improving human life is always in the spotlight of the scientific community, the Fifth Generation (5G) was conceived to improve not only the way humans interact with each other but also the way they interact with machines and the way machines interact among them. All use cases addressed in this generation are embedded in three main categories: Enhanced Mobile Broadband (eMBB), Ultra-Reliable and Low Latency Communications (URLLC), and massive Machine Type Communications (mMTC) [1], as seen in Fig. 1.1. The first one, eMBB, focuses on providing enormous data rate enabling applications such as video streaming, augmented reality and online gaming. The second one, URLLC, seeks to guarantee minimum latency and maximum reliability for applications related to autonomous cars and the industrial sector, among others. The third one, mMTC, aims to meet the growing needs of connectivity given the massive number of devices that require it for their proper functioning, e.g., cellphones, sensors, smart street lights, CCTV cameras, etc.

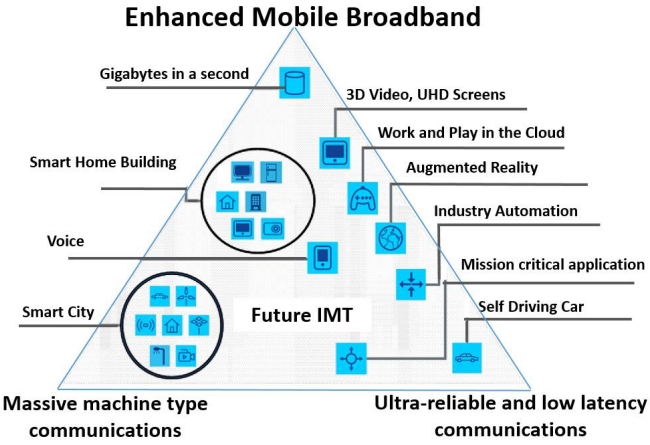

Figure 1.1: 5G usage scenarios [1].

In order to support the above mentioned use cases, some performance indicators should experience an improvement in 5G systems (also known as International Mobile Telecommunications (IMT) 2020 (IMT-2020) systems) compared

to previous generations (4G, also known as IMT Advanced (IMT-Advanced)). These indicators are:

- Peak data rate: Maximum achievable data rate under ideal conditions per user/device (in Gbit/s).
- User experienced data rate: Minimum achievable data rate per user/device in 95% of the coverage area (in Mbit/s or Gbit/s).
- Latency: The contribution by the radio network to the time from when the source sends a packet to when the destination receives it (in ms).
- Mobility: Maximum speed at which a defined QoS and seamless transfer between radio nodes that may belong to different layers and/or radio access technologies (multi-layer/-RAT) can be achieved (in km/h).
- Connection density: Total number of connected and/or accessible devices per unit area (per km^2).
- Energy efficiency: On the network side, energy efficiency refers to the number of information bits transmitted to/ received from users per unit of energy consumption of the radio access network (RAN) (in bit/Joule); on the device side, energy efficiency refers to the number of information bits per unit of energy consumption of the communication module (in bit/Joule).
- Spectrum efficiency: Average data throughput per unit of spectrum resource and per cell (bit/s/Hz).
- Area traffic capacity: Total traffic throughput served per geographic area (in $Mbit/s/m^2$).

Quantitatively, the improvement over IMT-Advanced is represented by the graph shown in Fig. 1.2.

Guaranteeing fulfillment of the new requirements demands higher bandwidths. In the bands below 6 GHz, bandwidths of tens of MHz are available. However, the mmW band can provide hundreds of MHz of continuous bandwidth, as shown in Fig. 1.3. The figure represents the bands at 24 GHz (24.25-24.45 GHz and 24.75-25.25 GHz), 28 GHz (27.5-28.35 GHz), 37 GHz (37-38.6 GHz), and 39 GHz (38.6-40 GHz), the Wi-Gig band (60 GHz) a new unlicensed band at 64-71 GHz [2]. In this context, the mmW band has been selected as a 5G enabler. It is included as an operating band in the technical specifications.

Nevertheless, despite the wide bandwidth spectrum offered by the mmW band, the high path loss and severe shadow fading inherent to the Super High

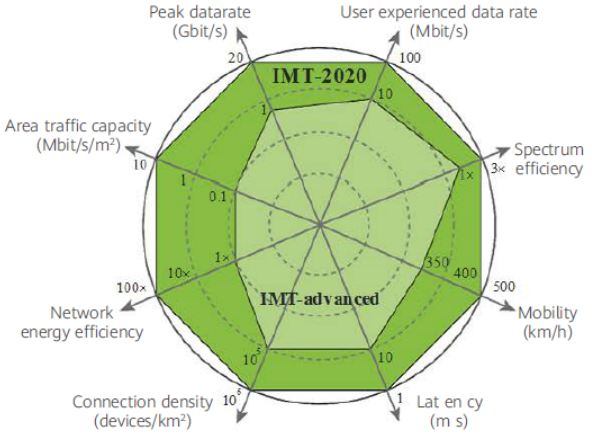

Figure 1.2: IMT-2020 versus IMT-Advanced [1].

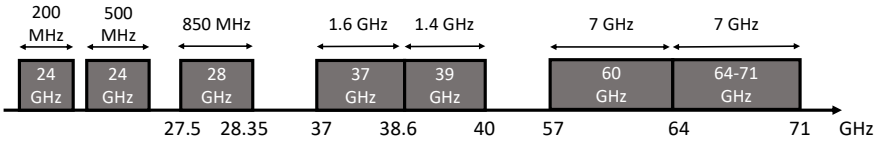

Figure 1.3: Bandwidth available at mmW bands.

Frequency (SHF) and Extremely High Frequency (EHF) bands (ranging from 3 GHz to 30 GHz, and from there to 300 GHz, respectively) are challenging. This fact opens new branches in the study of wireless propagation. The possibility of designing versatile antennas with multiple elements arises as the most evident way forward to compensate for such losses. An extreme case for this solution is massive MIMO [3], in which very large antenna arrays are used at Base Stations (BSs) to serve several users simultaneously.

Massive MIMO systems, previously used in under 6 GHz frequencies, also seem to be a good solution for mmW frequencies. With deployments based on a vast number of antennas (at least ten times more antennas than users), huge data rates can be achieved as long as the Line of Sight (LoS) is guaranteed [4]. In indoor hot-spot scenarios, where most of the traffic is concentrated [5] and the physical characteristics of the scenario facilitate LoS conditions, the use of massive MIMO systems could be very suitable [4].

At this point, and knowing that the existence of LoS is very convenient at mmW, it would be very useful to deploy distributed systems [6], where antennas

can surround the users in such a way that no matter where the user is, there is at least one transmission/reception point in sight. One example of these distributed systems is cell-free massive MIMO [7], commonly combined with a user-centric approach [8, 9]. This architecture consists of many remote radio transmission/reception points, better known as Access Points (APs), connected to a Central Processing Unit (CPU) that coherently serves a much smaller number of User Equipments (UEs) where there are no cell limits.

1.2 Review of the state of the art

The performance of systems based on a cell-centric design has always been limited by the interference experienced by users at cell borders. New applications for 5G and beyond require seamless deployments to ensure uniform service over the entire area. Considering the previous ideas, the most natural solution is to design user-centric cell-free systems. In this context and considering massive MIMO as one of the enabling technologies of next-generation systems, cell-free massive MIMO [7] is proposed.

Normally, when talking about cell-free massive MIMO, an AP is where the Channel State Information (CSI) is acquired through uplink pilot signals sent by the UEs and then used in the design of precoders. Furthermore, in the APs, the signal is multiplexed/de-multiplexed, converted by the analog/digital and digital/analog converters, and processed by the Base Band (BB) unit. On the other hand, the CPU coordinates all APs, and only payload data and power coefficients are transmitted between the CPU and APs.

However, some challenges arise when implementing cell-free massive MIMO. First, since all APs must be connected to the same CPU via front-haul, the system must withstand considerable traffic and signaling. This problem can be tackled via a user-centric approach so that a given UE is served by a subset of APs close to it that share a CPU, helping to relax the front-haul performance requirements significantly [8]. The design of clustering strategies both from the UEs' point of view and from the APs' point of view to have a scalable system is currently under discussion.

On the other hand, the massive deployment of antennas with their respective links to the CPU can easily become unmanageable. Faced with this problem, recently, cell-free massive MIMO systems based on serial front-haul links, where a single front-haul link feeds multiple APs, are being discussed as a means to simplify the deployments, among other reasons. However, the power consumption models used for cell-free massive MIMO deployments assume dedicated front-haul links. This being said, it is presumed that there is a need for

power consumption models that are better adjusted to the network's physical topology.

Going to the signal processing field, the proposed mmW massive MIMO systems for 5G communications [10] demand reliable estimation of the propagation channel to decide the precoders effectively to be used in each moment [11]. Special attention should be paid to modeling the propagation mechanisms such as transmission, scattering, and diffraction since they differ considerably from under 6 GHz frequencies to high frequencies [12].

In the following subsections, the points discussed above such as network topology, channel modeling for mmW bands and precoder design and resource allocation will be discussed in more detail.

1.2.1 Network topology

Logical topology

Cell-free massive MIMO systems, in their canonical form, rely on the cooperation of all APs to serve the users. Of course, this is not scalable. For this reason, different clustering alternatives have been studied both from the user point of view and from the AP point of view to improve the system's scalability [13, 14].

In [13], Keyvan Zarifi *et al.* proposed the network partitioning in virtual reconfigurable subsets. In one of the proposed solutions, subsets are defined so that interference caused by one AP to users served by another AP in the same subset is minimized. In this way, multiple partitions can be defined, forming different subsets of APs for each one. Subsequently, users are scheduled temporally, considering the partition that benefits them the most.

On the other hand, cell-centric and user-centric clustering have been proposed for its implementation at the same time in [14]. The APs are grouped in predefined clusters, and each cluster is connected to a CPU. Then, a user can select several APs from different clusters, which implies that the involved clusters cooperate to serve that user with all their APs. This solution allows more users to be scheduled simultaneously, translating into a higher instantaneous data rate. New clustering solutions are investigated to boost the cell-free massive MIMO systems' scalability.

Physical topology

The network's physical topology is a very important parameter to consider, even more, when the number of antennas to deploy is massive, as cell-free massive MIMO claims. In the first approach, the cell-free massive MIMO network is depicted as a group of APs connected through individual links to a unique

CPU. However, this can be a challenge from an aesthetic point of view and very laborious for installers and network maintenance operators. Sequentially distributed systems are a good way to avoid this. Specifically, the radio stripes [15, 16] designed by Ericsson are a solution to deploy cell-free massive MIMO systems in the near future.

1.2.2 Propagation channel models for mmW cell-free massive MIMO

Channel modeling is a fundamental step in modeling any wireless communications system since it determines to a certain extent how close to reality the results obtained are and, therefore, the conclusions derived from them. Specifically, at mmW, where the wavelength is quite small (in the order of tens of millimeters), the modeling of the channel becomes challenging since even imperfections on the surfaces of building structures or objects may affect signal propagation.

So far, most studies for cell-free massive MIMO systems consider channels of stochastic nature [7, 8, 14–21] and some other works consider simplified clustered channel models [9, 22, 23]. However, when studying specific use cases where the scenario is known, it is advisable to use deterministic channel models and thus minimize the impact of estimation errors on precoder design and planning decisions.

Several channel models have been designed for mmW communications. Some of them are listed below:

- 3GPP [24]: The model proposed by the Third Generation Partnership Project (3GPP) is valid for frequencies between 0.5 GHz and 100 GHz. The scenarios supported by the model are urban microcell street canyon, urban macrocell, indoor office, rural macrocell, and indoor factory. The model also supports mobility and spatial consistency.

- METIS [25]: Different channel model approaches are provided (map-based, stochastic, and hybrid models). The frequency range considered goes from 2 GHz to 60 GHz.

- mmMAGIC [26]: The model is based on the 3GPP model. It is focused on modeling the frequency dependence of large-scale parameters, ground reflections, intra clusters parameters, small-scale fading, blockage, and building penetration, among others.

- NYU Wireless [27]: It is a statistical spatial channel model. Multiple measurement campaigns were conducted on frequencies ranging bet-

ween 28 GHz and 73 GHz for indoor and outdoor environments. Omni-directional and directional antennas are considered.

- QuaDRiGA [28]: The model considers quasi-deterministic extensions to support spatial consistency and tracking of users. Extensive radio channel measurements in the 6-100 GHz range were taken to parameterize the model.

- IEEE 802.11ad/ay [29] : These semi-deterministic models are based on ray-tracing techniques. They focus on short-range communications for scenarios such as conference rooms, cubicles, and living rooms at 60 GHz. For modeling propagation losses, ray-tracing algorithms calculate the specular components, and the components due to diffractions, diffuse scattering, and transmission are aggregated in a stochastic way. The human blockage is also considered in terms of blockage probability and blockage attenuation.

- MiWEBA [30]: It consists of a quasi-deterministic channel model for 60 GHz. The model focuses on university campus, street canyon, hotel lobby, backhaul, and Device-to-Device (D2D) scenarios. It addresses several challenges such as spatial consistency and shadowing.

1.2.3 Design of precoders and power allocation

One of the mainstays of mmW massive MIMO systems is the signal steering in narrow beams to concentrate most of the power in a given direction. Having said that, it is evident that beamforming techniques are essential at mmW frequencies. How to achieve the optimum beamforming design is challenging. Analog beamforming is the simplest to implement, but the phase shifters can only be adjusted to form one angular beam, limiting the number of users served at a time. On the other hand, hybrid beamforming has a middle implementation complexity between the analog and digital approaches. However, despite being able to create multiple angular beams, the hybrid approach can only transmit one phase per signal and the same power on all antenna elements. This latter issue reduces the possibility of using power allocation strategies. Digital beamforming offers full flexibility, giving the chance to transmit any signal via any antenna element. In this Thesis, the digital beamforming concept in mmW massive MIMO systems will be referred to as precoding since in massive MIMO precoding concept is used to define a fully digital implementation [31].

It is worth mentioning that the research community in the past years has shown a certain reluctance to fully digital techniques due to the hardware

implementation complexity. Notice that for massive MIMO antenna arrays, the design of fully digital transceivers implies as many RF chains as antenna elements, which in most cases involves high power consumption. Nevertheless, low-power consumption fully digital approaches are arising [32], encouraging in-depth research on optimal precoding techniques for massive MIMO mmW systems. Precoding techniques should meet two main requirements: avoid interference and continuously adapt to the sudden channel changes in indoor scenarios.

In the case of fully digital approaches, data processing is only applied to the baseband signal, significantly reducing the complexity in the design of the baseband weighting matrix. In this sense, with the Maximum Ratio Transmission (MRT) technique [33], the baseband weighting matrix is optimized to maximize the received signal at the user's site. In contrast, the Zero Forcing (ZF) technique [34] can be applied to minimize interference. Moreover, precoding techniques mainly based on codebooks are possible. Thus, codebooks could be designed according to propagation conditions.

One step forward, the optimization of the power control coefficients has been studied in [17–19]. The constraints under which the problem is analyzed vary depending on the use case and the interest of each author.

In [17], the authors studied power optimization algorithms for both cell-free massive MIMO systems and Small Cell (SC) systems. Sub-optimal power allocation solutions are proposed based on MRT and ZF precoders. The results show that higher rates are achievable when implementing cell-free massive MIMO systems instead of SC systems. In [18], the power coefficients are also optimized but this time looking forward to satisfying per-user Quality of Service (QoS) and per-AP transmit power constraints when maximizing the energy efficiency in the downlink. In this work, the authors also considered the case where the CSI is not perfectly known.

Moreover, local computation of the precoder coefficients has been presented as a solution for scalability problems [19]. Local partial ZF and local protective partial ZF are precoding schemes that, according to the authors, can improve the values of Spectral Efficiency (SE) achieved with MRT or ZF precoding for distributed systems such as cell-free massive MIMO. Additionally, two different power allocation schemes are described and applied in [19]: Max-Min Fairness (MMF) and distributed heuristic channel-dependent strategy.

To improve the system's overall energy efficiency, not only power-saving solutions for the downlink have been studied, but also solutions for the uplink. In this sense, some mechanisms for controlling the power emitted from the user side have been proposed in [20, 21]. Concretely, in [20], the authors focused on the optimization in the selection of pilot powers to mitigate the pilot contamination. In consequence, higher throughputs are achieved when implementing

the proposed solution. Moreover, in [21] a max-min Signal to Interference plus Noise Ratio (SINR) problem is solved by optimizing the power coefficients in the uplink. The solution outperformed the existing algorithms considerably in terms of the per-user rate.

So far, the works above were carried out for under 6 GHz frequency bands. However, the energy efficiency maximization for cell-free massive MIMO systems at mmW has also been investigated in [22, 23]. In [22], the authors addressed the problem by considering hybrid precoding architectures. The results obtained demonstrated the increase of energy efficiency concerning uniform power allocation schemes but also a considerable performance degradation when compared with fully-digital precoding solutions. On the other hand, to reach higher energy efficiency values for cell-free massive MIMO systems, AP sleep-mode strategies have been studied [23], being their objective to switch on/off the APs according to the users' behavior for saving power, hence maximizing energy efficiency.

1.2.4 References summary of the state of art

Table 1.1 summarizes the above mentioned references which are classified according to the network topology studied, the channel model used and the precoding/combining technique implemented or designed.

1.3 Open problems

After reviewing the state of the art, it is clear that new methods are required to enhance channel estimation to reach the full potential of cell-free massive MIMO systems. Moreover, the trade-off between centralization and the subsequent optimum precoding calculation and distribution of calculations is to be further analyzed in the direction of optimizing the clustering of AP with a holistic view of the system as a whole.

Another open problem is the design of highly reliable and highly capable links between the CPU and the APs since it is a clear prerequisite to being able to make the most of the massive MIMO concept. Moreover, better performance can be achieved regarding peak data rates, reliability, and supported several UEs when massive MIMO is integrated with other beyond 5G enabling technologies, including, of course, the integration in the mmW band, which creates a plethora of problems to deal with.

This thesis arises from the confluence of the challenges previously identified, i.e., the impact of the physical and logical network topology on the system

Table 1.1: Summary of the state of the art.

Ref.	Network topology	Channel model	Precoding/combining technique
[7]	SCs and canonical cell-free massive MIMO with dedicated front-haul links	Stochastic (Independent Rayleigh fading channel)	MRT in Downlink (DL) and Matched Filtering (MF) in Uplink (UL)
[8]	User centric cell-free massive MIMO with dedicated front-haul links	Stochastic (Independent Rayleigh fading channel)	MRT in DL
[9]	User centric cell-free massive MIMO with dedicated front-haul links	Clustered channel model	Hybrid analog-digital partial ZF in DL
[14]	Distributed scalable cell-free massive MIMO with dedicated front-haul links	Stochastic (Independent Rayleigh fading channel)	MRT in DL using local CSI
[15]	Ubiquitous cell-free massive MIMO with sequential front-haul	Stochastic (Independent Rayleigh fading channel)	MRT in DL
[16]	canonical cell-free massive MIMO with sequential front-haul	Stochastic (Independent Rayleigh fading channel)	Normalized linear minimum squared error combining in UL
[17]	SCs and canonical cell-free massive MIMO with dedicated front-haul links	Stochastic (Independent Rayleigh fading channel)	MRT and ZF in DL
[18]	Canonical cell-free massive MIMO with dedicated front-haul links	Stochastic (Independent Rayleigh fading channel)	ZF in DL
[19]	Cell-free massive MIMO with several CPUs and dedicated front-haul links	Stochastic (Independent Rayleigh fading channel)	Local Partial ZF
[20]	User centric cell-free massive MIMO with dedicated front-haul links	Stochastic (Independent Rayleigh fading channel)	MRT in DL
[21]	Canonical cell-free massive MIMO with dedicated front-haul links	Stochastic (Independent Rayleigh fading channel)	Novel receiver filter in UL
[22]	User centric cell-free massive MIMO with dedicated front-haul links	Extended clustered statistical channel model	Hybrid analog-digital partial ZF in DL
[23]	Canonical cell-free massive MIMO with dedicated front-haul links	Simplified clustered channel model	Hybrid analog-digital with ZF for DL and UL

feasibility and performance, the realistic channel modeling and the precoder design, and the power allocation in mmW cell-free massive MIMO systems.

1.4 Hypothesis and objectives

As derived from the former sections, there is a gap between the theoretical benefits of mmW cell-free massive MIMO systems and their effective practical implementation. Thus, three main problems to solve have been identified: the impact of the network topology, the realistic channel modeling at mmW, and the precoding optimization in realistic scenarios. From these problems, the following hypotheses emerge:

- Hypothesis 1: Cell-free massive MIMO systems are not scalable in their canonical approach.

- Hypothesis 2: Power consumption modeling should adapt to the network's physical topology.

- Hypothesis 3: Scenario modeling affects the channel modeling.
- Hypothesis 4: The optimal precoders will depend on the accuracy of the scenario and channel modeling.

Under these hypotheses and the state-of-the-art analysis, the general objective of this Thesis is: to address network topology and signal processing problems in mmW cell-free massive MIMO systems for realistic indoor scenarios.

This global objective is further divided into the following specific objectives for the research:

- To propose a new solution for the scalability problem in cell-free massive MIMO systems.
- To design a power consumption model that considers the serial topologies' particularities.
- To develop a tool that allows characterizing indoor radio environments with sufficient precision for the design of radio algorithms and, at the same time, taking into account the actual environment under analysis.
- To assess the performance of state-of-the-art precoding algorithms and to fix the optimum attainable performance.
- To design precoding optimization algorithms that fit the demands of realistic scenarios.

1.5 Thesis outline

The Thesis is divided into six chapters. The first chapter is the introduction and the last chapter concludes the work and presents the future research lines. A brief description of the rest of the chapters is provided below:

Chapter 2 addresses the scalability problem in cell-free massive MIMO systems. Firstly, the received power modeling in ultra-dense networks is tackled, since it is relevant to determine whether AP should be included in a cluster or not based on its contribution to the whole system. Secondly, different clustering approaches are studied. Finally, clustering solutions that guarantee the feasibility of the cell-free massive MIMO are proposed.

Chapter 3 analyses the main differences between dedicated and serial front-hauls in terms of power consumption. From this analysis, some modifications to current power consumption models are proposed in order to get

more accurate results for serial front-haul serial architectures in cell-free massive MIMO.

Chapter 4 studies the realistic channel modeling at mmW. The influence on the radio channel of the modeling of the human body as well as of the scenario and the objects present in it, is analyzed. Additionally, a deterministic channel simulation is presented. Finally, a sensitivity analysis of the scenario modeling realism is carried out, highlighting the importance of considering furniture and scenario material in the modeling of indoor environments at mmW.

Chapter 5 deals with the precoding optimization in realistic scenarios. For this purpose, a use case with specific demands is presented. Then, the case problem is modeled as an optimization problem and the solution methodology is proposed. Finally, the performance results are discussed, demonstrating that realistic problems could be solved with the proper precoding design.

1.6 List of publications

The work developed during this Thesis made possible the following publications.

Journals

[J1] **D. Prado-Alvarez**, A. Antón, D. Calabuig, J. F. Monserrat, S. Bazzi and W. Xu, "Received power modelling in ultra-dense networks," in Electronics Letters, vol. 58, no. 11, May 2022.

[J2] **D. Prado-Alvarez**, D. Calabuig, J. F. Monserrat, S. Bazzi and W. Xu, "Study of access point clustering alternatives for scalable cell-free massive MIMO," IEEE Access, under review.

[J3] **D. Prado-Alvarez**, S. Inca, D. Martín-Sacristán and J. F. Monserrat, "Power consumption model for cell-free massive MIMO deployments with serial front-hauls," IEEE Access, under review.

[J4] **D. Prado-Alvarez**, S. Inca, D. Martín-Sacristán and J. F. Monserrat, "Millimeter-wave Human Blockage Model Enhancements for Directional Antennas and Multiple Blockers," in IEEE Communications Letters, vol. 25, no. 9, pp. 2776-2780, Sept. 2021.

[J5] **D. Prado-Alvarez**, S. Inca, D. Martín-Sacristán and J. F. Monserrat, "Sensitivity analysis of modeling realism for indoor scenarios at mmW band", IEEE Access, under review.

Other publications related with the Thesis

[R1] D. Martín-Sacristán, C. Herranz, J. F. Monserrat, A. Szczygiel, N. P. Kuruvatti, D. García-Roger, **D. Prado-Alvarez**, M. Boldi, J. Belschner, and H. D. Schotten, "5G Visualization: The METIS-II Project Approach," Mobile Information Systems, vol. 2018, Sept. 2018.

[R2] S. Inca, **D. Prado-Alvarez**, D. Martín-Sacristán and J. F. Monserrat, "Channel Modelling based on Game Engines Light Physics for mmW in Indoor Scenarios," in *14th European Conference on Antennas and Propagation (EuCAP)*, March 2020, pp. 1–5.

[R3] S. Inca, **D. Prado-Alvarez**, D. Martín-Sacristán and J. F. Monserrat, "Comparison of Optimization Methods for Aerial Base Station Placement with Users Mobility," in *European Conference on Networks and Communications 2019 (EuCNC 2019)*, Jun. 2019, pp. 1–5.

Chapter 2

Scalability in cell-free massive MIMO

In response to the high capacity demand of future communication systems, the deployment of ultra-dense networks with a massive number of antennas has emerged as a potential solution [35]. In this context, cell-free massive Multiple-Input Multiple-Output (MIMO) has been defined as an implementation of massive MIMO in an ultra-dense network with a considerably higher amount of Access Points (APs) than User Equipments (UEs). The APs are distributed over a wide area, and connected to a single Central Processing Unit (CPU) via front-haul, which controls network synchronization, power allocation, data throughput, etc. Each AP and UE can have one or more antennas [36]. The user-centric vision of cell-free massive MIMO [9], guarantees that the UE connects to a certain number of the surrounding APs, or to all of them in the case of canonical cell-free massive MIMO [14].

Generally, in deployments of Small Cells (SCs) or even in cell-free massive MIMO, maximum receiver gain is assumed, i.e., the receiving antenna is assumed to be perfectly oriented towards the transmitting antenna, as can be deduced from [7, 15]. However, although the error generated by this simplification is acceptable in some cases, the same cannot be valid for ultra-dense deployments when the total signal/interference received by the APs or the UEs is considered. In fact, it will be shown in this chapter that, if perfect orientation is assumed, some APs partially block the transmitted signal to other APs in the uplink of sufficiently large ultra-dense scenarios.

This chapter addresses the modeling of received power for ultra-dense systems, specifically, for the uplink of cell-free massive MIMO in indoor environments with ceiling-mounted APs. The main objective is to raise awareness

of the implications of considering maximum receiver gain in such systems. In this regard, an approach is proposed to consider the effective area of the receiver antenna. Finally, a comparison is done with the approach considering the radiation pattern of the receiver antenna.

On the other hand, some challenges arise when implementing cell-free massive MIMO. First, since all APs must be connected to the same CPU via front-haul, the system has to withstand a considerable amount of traffic and signalling. This problem can be tackled via a user-centric approach, so that a given UE is served by a subset of APs close to it that share a CPU, helping to relax the front-haul performance requirements significantly [8]. The design of clustering strategies both from the UEs' point of view and from the APs' point of view in order to have a scalable system is a topic currently under discussion. The clustering strategies can be classified in two groups depending on the means used to improve the performance of the system: applying interference cancellation or avoiding edge effects. In this work, these two approaches are analyzed by comparing them under different scenarios in order to find out what would be the most suitable under certain circumstances.

2.1 Received power modeling in ultra-dense networks

For the sake of clarity, the received power model is firstly introduced. According to Friis free space propagation model, the received power, P_r, can be calculated as

$$P_r = \frac{P_t G_t G_r}{\left(\frac{4\pi d}{\lambda}\right)^2}, \tag{2.1}$$

where P_t is the transmitted power, G_t is the gain in transmission, G_r is the gain in reception, d is the distance between transmitter and receiver, and λ is the wavelength.

Unless otherwise stated, it is generally assumed that G_t and G_r equal 1 in system level simulations. This assumption is valid when the transmitter, equipped with an omnidirectional antenna, and the receiver are perfectly oriented towards each other. However, even considering perfect orientation, if APs are closely deployed, and relatively far APs are considered for the received signal power computation, it is easy to find APs that produce a shadow onto further APs (not related to shadowing modeled by the slow fading). This effect is depicted in Fig. 2.1. As a consequence, Receiver 2 in Fig. 2.1 cannot actually receive all the power defined in (2.1), which in turn leads to an overestimated received power.

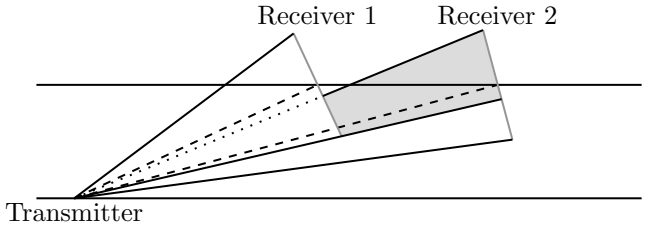

Figure 2.1: Shadow effect of Receiver 1 onto Receiver 2, for perfectly oriented receivers towards the transmitter.

Towards obtaining a more realistic model, the antennas should be considered parallel to the ceiling and then, the corresponding fraction of the received power should be modeled. With this aim, in Section 2.1.1, two approaches to consider the receiver gain are analyzed.

2.1.1 Alternative approaches considering the reception gain

In this work two approaches considering G_r are analyzed. The first considers the radiation pattern of the receiver antennas, and the second takes the effective area of the receiver antennas into account.

Radiation pattern approach

The radiation pattern approach consists of the modeling of G_r as a function of the angle of arrival of the signal, θ. $G_r(\theta)$ takes values such that for $|\theta_1| \leq |\theta_2|$, $G_r(\theta_1) \geq G_r(\theta_2)$. With this radiation pattern, if the receiver antennas are fixed to the ceiling in an indoor scenario, and the beam is steered to the ground, i.e., $\theta = 0$ corresponds to the direction perpendicular to the ground, the maximum gain is achieved below the antennas, and this gain becomes smaller as the distance to the antenna increases until it reaches the minimum gain. This is because θ increases with the distance.

Effective area approach

In this section, another approach is presented to include, in the system model, a variable gain in reception with respect to the angle of arrival. In particular, it is proposed to integrate the effective area into the pathloss model. The effective area is modeled at the receiver as the projection of the physical area in the direction of the transmitter (see Fig. 2.2).

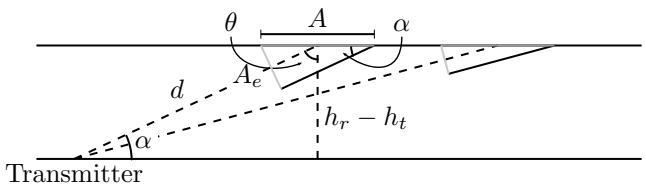

Figure 2.2: Cross-section of a scenario with one transmitter and two receivers and representation of the effective area.

Mathematically, A_e can be derived through the following equations:

$$\sin\alpha = \frac{h_r - h_t}{d} = \frac{A_e}{A}, \tag{2.2}$$

$$A_e = A\frac{h_r - h_t}{d},\ h_r > h_t, \tag{2.3}$$

where $\alpha = \frac{\pi}{2} - \theta$ is the angle of departure from the transmitter with respect to the floor's normal, h_t and h_r are the heights of the transmitter and receiver respectively, d is the distance between them, and A is the physical area of the receiver antenna. Then, the gain at the receiver antenna can be computed as

$$G_r = \frac{A_e}{A} = \frac{h_r - h_t}{d}. \tag{2.4}$$

Finally, using (2.4), (2.1) can be expressed as

$$P_r = \frac{P_t G_t}{\left(\frac{4\pi}{\lambda}\right)^2 d^3}(h_r - h_t). \tag{2.5}$$

Comparing (2.5) with (2.1), it can be noticed that, in (2.5), G_r is replaced by a constant, $h_r - h_t$, and an increase by 1 of the distance exponent. Therefore, with this approach, G_r can be easily included in the pathloss model.

2.1.2 Alternatives Comparison

In order to analyze qualitatively and quantitatively the effect of considering G_r, the following evaluation scenario is proposed. The scenario consists of a squared room where a network of APs is installed on the ceiling. The APs are equi-spaced with an intersite distance $r = 5$ m. Additionally, there is one UE in the center of the scenario transmitting to all APs at the same time with P_t equal to 21 dBm. The heights are 6 m and 1.5 m for the APs and the UE

respectively. These heights are typical for indoor industrial scenarios as stated in [15, 37]. The evaluation is carried out for different scenario dimensions ranging from a 10×10 m^2 scenario up to 10,000×10,000 m^2. The scenario side length is denoted as D, as it can be seen in Fig. 2.3.

For the radiation pattern alternative, $G_r(\theta)$ is modeled with the antenna element radiation pattern used in [38], without considering any tilt. Thus, the receiving antenna gain is modeled as

$$G_r(\theta) = -min\left[12\left(\frac{\theta}{\theta_{3dB}}\right)^2, G_{r_m}\right], \tag{2.6}$$

where θ_{3dB} is the beam width of the radiation pattern. Following the typical case used in [38], θ_{3dB} is assumed to equal 70 degrees and $G_{r_m} = 20$ dB. Figure 2.4 shows the radiation pattern.

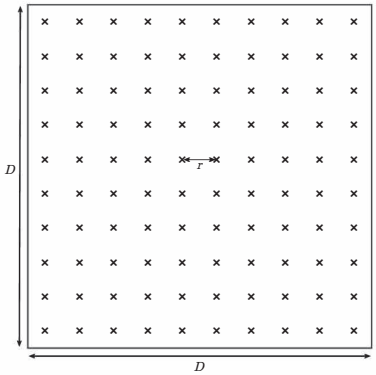

Figure 2.3: Scenario layout for $D = 50$ m and $r = 5$ m.

In this work, the pathloss model for free space based on the Friis equation has been considered. Therefore, it is possible to study the modeling of the received power avoiding to consider other effects of different nature that are taken into account when obtaining the empirical models. The evaluation is carried out in uplink, i.e., in this case the transmitting antenna is the UE's antenna and the receiving antennas are those of the APs.

Figure 2.5 presents 3 curves which show how the total received power at the APs increases with the size of the scenario when considering $G_r = 1$, the radiation pattern or A_e. As it can be noticed, the solid line ($G_r = 1$) does not converge even for scenarios as large as 10,000×10,000 m^2. This implies that at a certain point, according to the model, more power could be received than

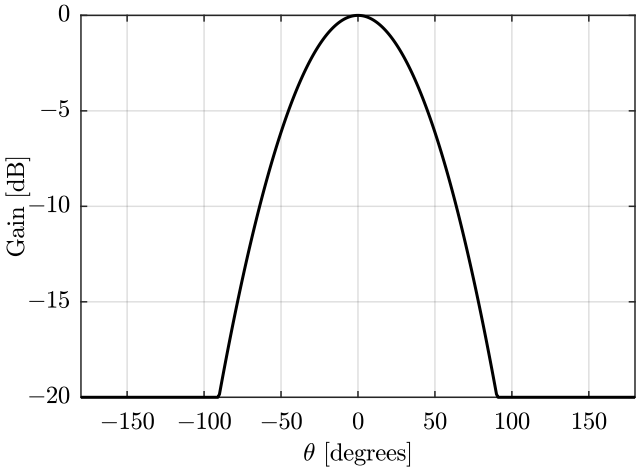

Figure 2.4: Radiation pattern.

transmitted, which is completely impossible in practice. Although significantly reduced, this effect is also present in the approach that considers the radiation pattern. This is due to the minimum gain of -20 dB considered in the radiation pattern in (2.6), and illustrated in Fig. 2.4, which implies that the curve for the radiation pattern can never be below -20 dB from the curve for $G_r = 1$. Finally, for the approach where A_e is considered, the curve converges.

To illustrate with another example the consequences of considering one of these approaches, the number of APs where 95% of the power is received is determined for different scenario sizes. A similar criterion has been followed for downlink in [15] to determine the APs that provide the 95% of the power to a particular UE. Figure 2.6 presents 3 curves which show how the number of selected APs increases when considering $G_r = 1$, the radiation pattern or A_e. Similarly to the previous analysis, the curve for $G_r = 1$ grows rapidly without reaching a convergence point. Furthermore, although Fig. 2.5 gives the impression that the curve for the radiation pattern will soon converge, the graph in Fig. 2.6 shows that the number of APs selected continues to grow significantly even for the largest scenarios considered. Finally, the only curve that converges is that of the approach that considers A_e.

Analyzing the two figures at the same time, it can be concluded that: (i) when considering maximum gain in reception, the received power and the number of APs where it is concentrated increase rapidly with respect to the size of

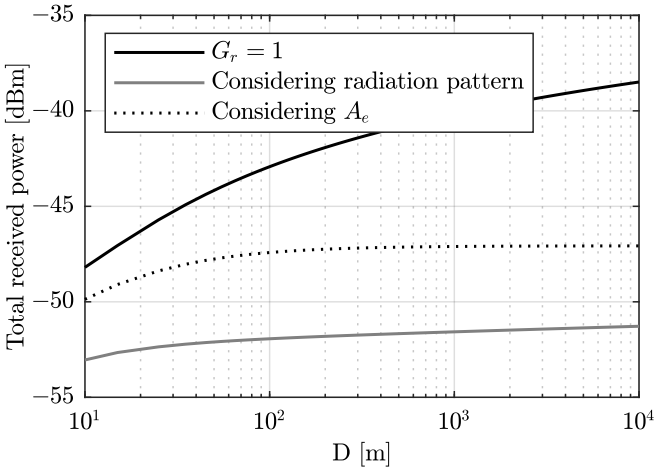

Figure 2.5: Total received power for all alternatives.

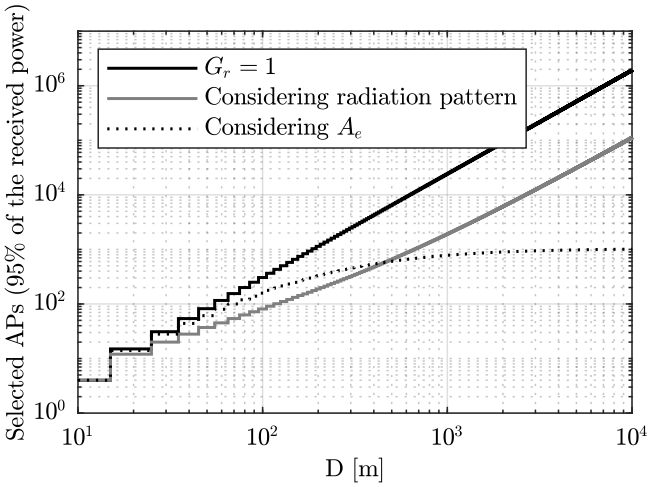

Figure 2.6: Selected APs for all alternatives.

the scenario; (ii) for the solution considering the radiation pattern of the receiving antennas in uplink, the curves grow considerably slower than in the $G_r = 1$

case, although they do not converge completely; and (iii) when considering the effective area, both the received power and the selected APs converge.

Hence, taking into account these results, the proposed model is used in the following sections of this chapter.

2.2 Scalability problem

Cell-free massive MIMO systems, in their canonical form, rely on the cooperation of all APs to serve the UEs. This implies that, as the network grows, so do the computational requirements of the network and the volume of data and signaling that has to be exchanged between each AP and each UE. Due to this, these systems are said to be non-scalable. A solution to this problem is to find other approaches with a similar performance that can be scaled with the network size. To do this, it is important to agree on the main features a scalable system should satisfy. Then, systems with such features could be designed. In [39], the authors state that the network is scalable if the following tasks have finite complexity and resource requirements for each AP as K tends to ∞:

1. Signal processing for channel estimation.
2. Signal processing for data reception and transmission.
3. Front-haul signaling for data and Channel State Information (CSI) sharing.
4. Power control optimization.

In [14], a solution was proposed and considered to be fully scalable. The solution is based on the definition of fixed clusters of APs, each of them connected to a different CPU. Each UE selects the best-server AP and a set of serving APs, up to a maximum quantity of APs. The CPU of the best-server is in charge of the channel estimation and the reception/transmission processing. This processing and channel estimation is done independently for each UE and taking into account only the serving APs. Therefore, even in the worst case (all UEs require the maximum amount of serving APs), the total resource requirements of this approach increases linearly with the amount of UEs in the network. When the network grows, all, the amount of UEs, APs, and CPUs grow with the same proportion and, hence, both the amount of UEs and the available resources grow with the same proportion. As a consequence, the system is scalable. However, this scalability claimed in [14] was questioned by

[39], since [14] does not explicitly limit the number of UEs that can connect to one AP.

This raises the question whether all the criteria in the scalability definition in [39] are necessary in practice. For instance, although one can argue the necessity of limiting the amount of UEs that can be served by one AP, the reality is that many works in the literature dealing with resource allocation problems do not consider this limitation. This is due to two main reasons. First, it is unlikely to saturate the APs by the amount of UEs, specially considering deployments with more APs than UEs like in cell-free massive MIMO systems. Second, real systems have access control mechanisms to avoid this situation. In this sense, we wonder whether it is reasonable to criticize the scalability of the solution in [14] because the amount of UEs served by one AP is not explicitly limited. From our point of view, the definition of scalability should take into account the system viability in terms of computation and resource requirements as the system increases in size.

To do this, it has been discussed first when a system is viable. In this context, viability can be defined using the system denial of service probability, i.e., the probability that a UE cannot be served by the system due to the lack of computational, front-haul or radio resources. In this sense, it can be said that a system is viable if the denial of service probability is below a maximum threshold, i.e., $P_{\mathrm{D}}(\mathcal{S}) \leq P_{\max} < 1$, where $P_{\mathrm{D}}(\mathcal{S})$ is the denial of service probability of system $\mathcal{S}$. Let $|\mathcal{S}|$ be the size of system $\mathcal{S}$, let $|\mathcal{S}_1| < |\mathcal{S}_2| < \ldots$, and let $\lim_{n\to\infty} \mathcal{S}_n = \mathcal{S}$, then we say that $\mathcal{S}$ is scalable if $P_{\mathrm{D}}(\mathcal{S}_n) \leq P_{\max}$ for all n.

Now a system that extends throughout an infinite plane, with certain density of APs and UEs, is considered. It can be defined a series of systems $\mathcal{S}_1$, $\mathcal{S}_2, \ldots$ that increase in size in the plane. For instance, they can be deployments inside squares with an increasing side length. In the case of canonical cell-free massive MIMO, a unique CPU manages the reception and transmission to all UEs, and collects CSI information from all APs. Taking into account that the CPU computational capabilities as well as the front-haul resources are limited, it is clear that $\lim_{n\to\infty} P_{\mathrm{D}}(\mathcal{S}_n) = 1$. This system is, hence, not scalable. Note that this conclusion is valid even if we provide the CPU with infinite computational capabilities, i.e., the front-haul still makes the system not scalable. In case APs are clustered to serve the UEs, the system is provided with certain density of CPUs. Each CPU manages an individual AP cluster and the UEs in that cluster. Therefore, $P_{\mathrm{D}}(\mathcal{S})$ depends on the probability that the CPUs and theirs APs run out of resources. If cooperation is avoided among CPUs, this probability does not depend on the system size. With a proper design of the CPU capabilities and the cluster size, this system is, hence, scalable.

Therefore, using the previous (less restrictive) definition of scalability, clustering ensures the scalability of the system, if cooperation between clusters is not allowed.

2.3 Clustering solutions

As shown in the previous section, the solution to guarantee scalability is self-presenting: divide and conquer. However, the division of the network into clusters and the posterior allocation of resources should be done in a smart way, trying to take full advantage of the flexibility of cell-free deployments and user-centric solutions. In this sense, this work focuses on the study of the strengths and weaknesses of current clustering solutions with the aim of proposing more advanced solutions to achieve better performance.

In what follows, two clustering alternatives are analyzed. The first alternative focuses on ensuring that the user is at the center of the cluster, thus avoiding edge effects. This is ensured by creating a cluster of APs for each individual UE. Due to this, each cluster of APs serves only one UE. The second alternative includes several UEs in each cluster of APs, and focuses on using interference cancellation techniques to reduce the effect of interference.

In the following sections, these two alternatives are compared in terms of sum data rate. For this purpose, first, the system model is defined. Then, different clustering techniques are analyzed for both uplink and downlink. Finally, conclusions are reached on the suitability of using one clustering solution or another, depending on the characteristics of the scenario and the inherent needs of each of the transmission modes.

2.4 System model

In this chapter, a scalable cell-free massive MIMO deployment is considered. The deployment consists of L single-antenna APs spatially distributed in the scenario, K single-antenna UEs, and M AP and UE clusters. The APs in the m-th cluster of APs serve the UEs in the m-th cluster of UEs. Let $\mathcal{L}_m$ be the set of APs in the m-th cluster, and let $\tilde{m}(k)$ be the cluster the k-th UE belongs to. Without loss of generality, we index the UEs in the same cluster continuously, i.e., the UEs in the m-th cluster are those with indices $\tilde{k}(m-1)+1$, $\tilde{k}(m-1)+2, \ldots, \tilde{k}(m)$, where $\tilde{k}(m)$ is the largest index of the UEs in the m-th cluster, and $\tilde{k}(0) = 0$. The channel between the k-th UE and the APs of the m-th cluster is denoted by $H_{km} \in \mathbb{C}^{|\mathcal{L}_m|}$, where $|\mathcal{L}_m|$ is the amount of APs in the m-th cluster.

$$R_k^{\mathrm{UL}} = \log \frac{|I + P\sum_{i=1}^{k} H_{i\tilde{m}(k)} H_{i\tilde{m}(k)}^{*} + P\sum_{i=\tilde{k}(\tilde{m}(k))+1}^{K} H_{i\tilde{m}(k)} H_{i\tilde{m}(k)}^{*}|}{|I + P\sum_{i=1}^{k-1} H_{i\tilde{m}(k)} H_{i\tilde{m}(k)}^{*} + P\sum_{i=\tilde{k}(\tilde{m}(k))+1}^{K} H_{i\tilde{m}(k)} H_{i\tilde{m}(k)}^{*}|}. \tag{2.7}$$

In order to model the two clustering alternatives exposed in the previous section with this model, interference cancellation techniques are used for the set of UEs in each cluster. In particular, some interference cancellation is performed between the UEs $1, 2, \ldots, \tilde{k}(1)$, also between the UEs $\tilde{k}(1)+1, \ldots, \tilde{k}(2)$, etc.

As a measure of comparison between the clustering alternatives considered in this work, the total sum data rate is calculated for both uplink and downlink. In the case of the uplink, Successive Interference Cancellation (SIC) [40] is considered in the decoding. This algorithm consists of (i) decoding the signal of the first UE considering the signal of the rest as interference, (ii) substracting the signal decoded from the first user from the received signal, (iii) decoding the signal of the second UE considering the signal from the third UE onwards as interference, and so on. This reception technique is known to be capacity achieving if all the sources of interference have a known covariance. Specifically, since the decoding order does not affect the sum rate [35], we assume that the first signal to be decoded is the one corresponding to the user with the highest index, i.e., the UE $\tilde{k}(m)$ of the m-th cluster, and then we follow the decreasing order of the indices. Therefore, the achievable data rate of the k-th UE in the uplink with an identity noise covariance is as shown in (2.7) at the beginning of next page, where P is the available power at the UEs. In (2.7), the interference has been divided in two terms according to its origin. In the numerator, the first term is the noise covariance; the second term includes the interference from UEs in clusters with indices $m < \tilde{m}(k)$, the interference from the UEs in the same cluster, and the signal of the k-th UE; and the third term includes the interference from the UEs in clusters with indices $m > \tilde{m}(k)$. In the denominator the terms are similar except by the fact the the signal of the k-th UE is not included.

Analogously, in the case of the downlink, Dirty Paper Coding (DPC) [41] is considered. This coding technique consists on adapting the codebooks of the transmitter to a known interference in such a way that the interference does not affect the achievable rate. Therefore, the CPU of the AP cluster can (i) encode the signal of the first UE, (ii) treat this signal as a known interference for the second UE, and so on. In this case, the first UE sees the signal from the other UEs as interference, the second UE sees the signal from the third UE onwards as interference, etc. As in the case of SIC, this encoding technique is known to

$$R_k^{\mathrm{DL}} = \log \frac{1 + \sum_{i=1}^{\tilde{k}(\tilde{m}(k)-1)} H_{k\tilde{m}(i)}^* Q_i H_{k\tilde{m}(i)} + \sum_{i=k}^{K} H_{k\tilde{m}(i)}^* Q_i H_{k\tilde{m}(i)}}{1 + \sum_{i=1}^{\tilde{k}(\tilde{m}(k)-1)} H_{k\tilde{m}(i)}^* Q_i H_{k\tilde{m}(i)} + \sum_{i=k+1}^{K} H_{k\tilde{m}(i)}^* Q_i H_{k\tilde{m}(i)}}. \quad (2.8)$$

be capacity achieving if all the sources of interference have a known covariance. Some works found an uplink-downlink duality when SIC and DPC are used [42]. In particular, the achievable rates are the same. In [42], it is shown that the DPC encoding order that achieves certain achievable rates is the reversed SIC decoding order of the dual uplink system. Following this principle, we assume that the encoding order is the reversed order considered for the uplink, i.e., the encoding follows the increasing order of the UEs' indices. Therefore, the achievable data rate of the k-th UE in the downlink with an identity noise covariance is as shown in (2.8) at the beginning of next page, where Q_k is the transmit covariance matrix of the k-th UE. In (2.8), the interference has also been divided in two terms according to its origin, and in a similar manner as in (2.7). Since single-antenna UEs are considered, it is not needed to include determinants in the equation.

2.5 Analysis of the clustering solutions for the uplink

In this section, a clustering solution for each of the two clustering alternatives described in Section 2.2 for the uplink is presented. Subsequently, the performance of the two solutions is studied in a particular scenario to gain insights into the performance of the two clustering alternatives.

2.5.1 User-at-center

This solution is part of the first clustering alternative in Section 2.2. Therefore, each UE is close to the center of a custom-designed cluster, and therefore does not experience edge effects. The clusters of different UEs can overlap. In [39], the clusters are formed according to the following procedure. The UE appoints the AP with the strongest large-scale fading channel coefficient as its master AP. The maximum amount of UEs that one AP can served is limited. So, when the UE requests the service, the AP will assign the channel it considers to be the least affected by interference from the other UEs it serves. The master AP informs a limited set of neighboring APs that it is going to serve this UE. In particular, the informed APs are those whose channel with the

UE is at most a "threshold" weaker than the channel of the master AP. Then, the informed APs decide whether they serve the UE or not. To make this decision, the APs have to take into account other UEs they are serving. Using this clustering solution, as many clusters as UEs are created, the latter being relatively centered in their respective clusters. This implies that the last UE of the m-th cluster is m, i.e., $\tilde{k}(m) = m$ and the cluster where the k-th UE belongs to is k, i.e., $\tilde{m}(k) = k$. Considering this, the achievable data rate of the k-th UE for uplink and downlink results in, respectively,

$$R_k^{\text{UL-UaC}} = \log \frac{|I + P\sum_{i=1}^{K} H_{ik}H_{ik}^*|}{|I + P\sum_{i=1,i\neq k}^{K} H_{ik}H_{ik}^*|}, \tag{2.9}$$

$$R_k^{\text{DL-UaC}} = \log \frac{1 + \sum_{i=1}^{K} H_{ik}^* Q_i H_{ik}}{1 + \sum_{i=1,i\neq k}^{K} H_{ik}^* Q_i H_{ik}}. \tag{2.10}$$

Since this clustering solution creates a different AP cluster for each UE, it is not possible to cancel interference between any of the UEs. Therefore, all the UEs of the scenario are considered interferers by the k-th UE.

2.5.2 Disjoint clusters

This solution is part of the second clustering alternative in Section 2.2. For this solution, the APs are grouped into non-overlapping clusters of a specific size, i.e., $|\mathcal{L}_m| = N$ for all m. Regarding the UE clusters, the clustering process is as follows. First, the UEs select their master APs as in the previous solution, i.e., the APs with the strongest large-scale fading channel coefficient. Then, the m-th UE cluster is composed of the UEs which master AP is in the m-th AP cluster. It is clear that, following this clustering process, the UE clusters are composed of several UEs in general. Therefore, since the signals of the UEs in the same cluster are processed by the same CPU, some interference cancellation technique could be used for the decoding/encoding. However, UEs are not prevented from suffering cluster border effects.

2.5.3 Comparison of solutions for uplink

In this section, the performance of the two previous clustering solutions is studied in a particular scenario. The scenario is a square of 32 by 32 ceiling-mounted APs in a squared grid with an inter-AP distance of 10 m. In order to avoid scenario border effects, a wrap-around technique is implemented. The heights of APs and UEs are 6 m and 1.5 m respectively. The channel model used is the "Industrial indoor scenario" in [15]. The UEs have 10 mW of

available power, and the noise power at the receivers is $1.5887 \cdot 10^{-10}$ mW, which corresponds to the noise power at 15 °C and a transmission bandwidth of 20 MHz. In this scenario, the AP clusters of the "disjoint clusters" (DC) solution are squared groups of APs located in a squared grid over the scenario.

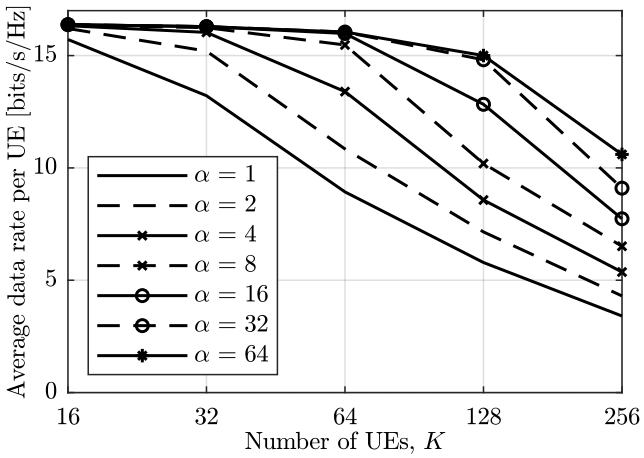

Figure 2.7: Achievable data rate in the uplink for different configurations.

First, the results for several configurations of the "user-at-center" (UaC) solution are obtained. From one configuration to the other the only parameter that changes is the maximum number of UEs that can be served by one AP, denoted by α. As it is shown in Figure 2.7, the average data rate per UE decreases as the number of UEs in the scenario increases. This decrement can be softened by allowing each AP to serve more UEs, i.e. by increasing α.

In the case of the UaC solution, the size of the AP clusters is variable. Assuming that the master AP of each UE informs all APs in the scenario to create the AP cluster of this UE, then all APs serve $\min(K, \alpha)$ UEs. Using this assumption, we can compute the average AP cluster size as $L \min(K, \alpha)/K$. For instance, in the case of 256 UEs and $\alpha = 16$, the average cluster size is $1024 \times 16/256 = 64$. In order to facilitate the comparison between the UaC solution and the DC solution for different cluster sizes, we will compare the data rate of certain average cluster size of the UaC solution with the data rate of the same cluster size of the DC solution.

Figure 2.8 shows the average data rate per UE versus the total number of UEs in the scenario for UaC and DC solutions for cluster sizes of 16, 64 and 256

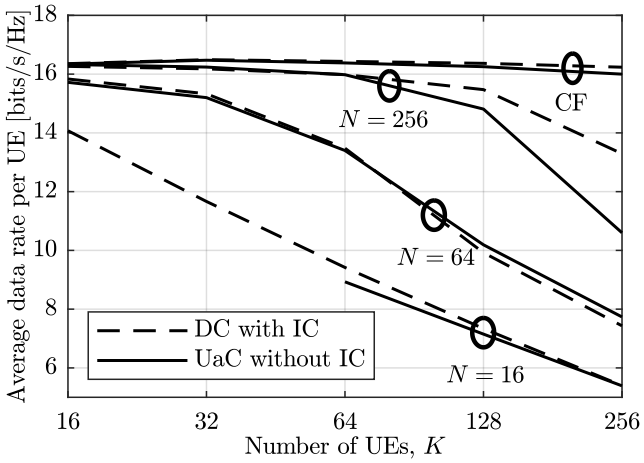

Figure 2.8: Achievable data rate in the uplink fixing the average cluster size.

APs. The figure also shows the average data rate for canonical cell-free massive MIMO with and without interference cancellation as a benchmark. In Figure 2.8, when cluster sizes of 16 APs and 64 APs or less than 64 UEs are considered, the compared solutions have a similar behaviour. However, when considering clusters of 256 APs and more than 64 UEs, the DC solution clearly outperforms the UaC solution. Objectively speaking, according to what it is shown, there is no solution whose performance prevails over the other for any number of UEs. This motivates the definition of a mixed solution in the following section.

2.5.4 Mixed solution for uplink

This solution is inspired by the idea of merging the best of the previous solutions: the avoidance of border effects and the possibility of applying interference cancellation. The UE and AP clustering is performed as follows. First, the APs are grouped into non-overlapping cluster cores, which are going to be at the center of the AP clusters. In particular, for the results in this section and for the same scenario described in the previous section, the AP clusters are squares of $\sqrt{|\mathcal{L}_m|} \times \sqrt{|\mathcal{L}_m|}$ APs, whereas the cluster cores are squares of $\sqrt{|\mathcal{L}_m|}/2 \times \sqrt{|\mathcal{L}_m|}/2$ APs at the center of the corresponding cluster, for $m = 1, \ldots, M$. Second, each UE is linked to its best-serving AP, as previously. The cluster of UEs served by each AP cluster is the set of UEs linked to the APs in the corresponding core.

In Figure 2.9, a cluster of 64 APs (black grid) and its core formed by the APs inside the red solid border square are depicted. Additionally, the cores of other tentative overlapping clusters are delimited by a red dashed border square. As a result, each AP cluster serves a UE cluster that is centered in the AP cluster. Moreover, this solution implies that each AP will be included in several AP clusters. The number of clusters depends on the ratio between the size of the cluster and its core. For instance, if the cluster has 64 APs and the core 16 APs, as represented in the figure, each AP of the cluster will be connected to 4 AP clusters, as is the case of the AP highlighted in gray.

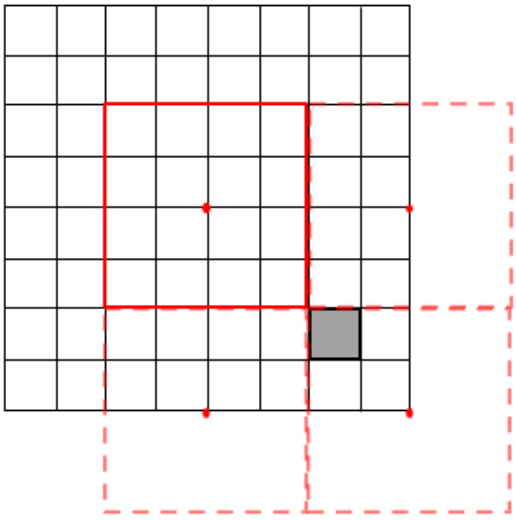

Figure 2.9: Mixed solution.

In Figure 2.10 the achievable data rate per UE for a cluster average size of 256 APs is shown for the UaC, the DC and the mixed solutions. The curve of the UaC solution, was obtained following the procedure explained for Figure 2.8. As it can be noticed, the performance with the mixed solution is better than the UaC and the DC solutions. Therefore, in this case, the best performance is not obtained by only (i) avoiding the cluster border effects or (ii) cancelling all the interference of UEs with the master AP in the cluster. In this case, a solution that mixes the two clustering alternatives is needed. In any case, the DC solution is the most similar to the mixed solution. This highlights the importance of cancelling interference.

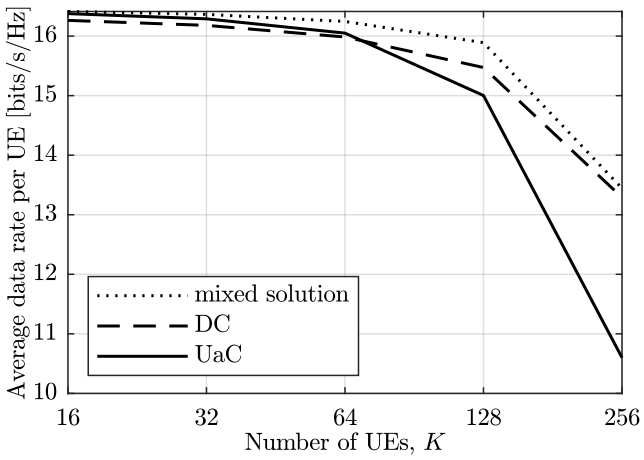

Figure 2.10: Achievable rate for mixed solution.

2.6 Analysis of the clustering solutions for the downlink

In the uplink, the APs can be considered passive receivers since they just need to send the signal received to the corresponding CPUs. However, in the downlink case, the APs are actively transmitting, so a certain amount of power needs to be allocated. This power allocation becomes more challenging if the clusters are overlapping. In that case, as each AP could be connected to more than one CPU, all the CPUs involved would have to cooperate, which could lead to a

non-scalable system. In the following sections, two clustering solutions, as well as the corresponding power allocation schemes, will be analyzed and compared.

2.6.1 User-at-center

According to [39], in the downlink, the AP clusters are created as explained in Section 2.5.1. Moreover, since the APs serve a maximum of α UEs, they split their available power into this amount of UEs, i.e., letting P be the available power at the APs, they use a maximum of P/α for each user [39]. The actual power used to transmit to the UEs is obtained by multiplying P/α by a normalized precoding vector, which, in the case of the k-th UE, is computed as

$$w_k = \frac{H_{kk}}{|H_{kk}|}. \tag{2.11}$$

Then, the power used by the l-th AP of the k-th cluster to transmit to the k-th UE is

$$\frac{P}{\alpha}|w_{kl}|^2 \leq \frac{P}{\alpha}, \tag{2.12}$$

which indicates that the total power used to transmit to the UEs by all APs is, indeed, P/α. This power allocation, which is proposed in [39], ensures the APs do not use more power than P, although in a very conservative way. In particular, in average, the APs use significantly less power than P to transmit to all the UEs. In order to illustrate this fact, we assume that each AP serves exactly α UEs. Then, the average amount of APs serving each UE is

$$L_{\text{serving}} = \frac{L\alpha}{K}. \tag{2.13}$$

As mentioned before, the total power used to transmit to each UE is P/α, which is split into the APs serving this UE. Therefore, the average power used per AP and UE is $P/\alpha L_{\text{serving}}$. Since the APs serve α UEs, the average total power used per AP is

$$\frac{P}{\alpha L_{\text{serving}}}\alpha = \frac{PK}{L\alpha}. \tag{2.14}$$

In order to illustrate this, let's put two numerical examples. If $\alpha = 4$, $K = 256$, and $L = 1024$, the total allocated power average would be $\frac{P}{16}$ and if $\alpha = 8$, $K = 64$, and $L = 1024$, the average drops to $\frac{P}{128}$. This conclusion is quite striking, as it shows that a large part of the power could be wasted.

2.6.2 Disjoint clusters

As in the case of the uplink, we can also consider the creation of disjoint clusters in the downlink with size $|\mathcal{L}_m| = N$ for all m. As discussed before, the resource allocation in each cluster should not be conditioned to the particular allocation performed in neighboring clusters. If not, the effect of each cluster would propagate throughout the scenario, making the resource allocation not scalable. In order to avoid this scalability problem, we propose to perform the resource allocation in each cluster as if they were isolated from the rest, i.e., assuming that the interference from the other clusters do not affect their UEs. Without loss of generality, we are going to particularize this resource allocation for the first cluster, i.e., $m = 1$. In this case, and taking into account that we neglect the interference from other clusters, the achievable rate of the k-th UE is, using (2.8),

$$R_k^{\text{DL-2}}(\{Q_i\}_{i=1}^{\tilde{k}(1)}) = \log \frac{1 + H_{k1}^* \left(\sum_{i=k}^{\tilde{k}(1)} Q_i\right) H_{k1}}{1 + H_{k1}^* \left(\sum_{i=k+1}^{\tilde{k}(1)} Q_i\right) H_{k1}}, \tag{2.15}$$

for $k = 1, \ldots \tilde{k}(1)$. The rate expression in (2.15) is the one used for the resource allocation, i.e., the computation of the transmit covariances $\{Q_i\}_{i=1}^{\tilde{k}(1)}$. However, the actual achievable rate is shown in (2.8), which takes all the interference into account. The latter expression is the one used in the following section to compute the achievable rate in the figures.

To obtain the transmit covariances, we propose to maximize the sum data rate in the cluster taking into account the limited available power in the APs. Mathematically, for the cluster $m = 1$, we want to solve

$$\begin{aligned} \max_{\{Q_k\}_{k=1}^{\tilde{k}(1)}} & \sum_{k=1}^{\tilde{k}(1)} R_k^{\text{DL-2}}(\{Q_i\}_{i=1}^{\tilde{k}(1)}), \\ \text{s.t. } & Q_k \succeq 0, \ k = 1, \ldots, \tilde{k}(1), \\ & \sum_{k=1}^{\tilde{k}(1)} q_{kl} \leq P, \ l = 1, \ldots, N, \end{aligned} \tag{2.16}$$

where q_{kl} is the l-th element of the main diagonal of Q_k. To solve this problem, we can use the algorithm proposed in [43], which is based on [44]. In [43], the Broadcast (BC) weighted sum rate maximization problem under several linear power constraints is solved by iterating between one "outer problem" and an "inner problem". With the optimum transmit covariance matrices of (2.16), the APs use all their available power. It is worth recalling that this solution

is optimum locally, i.e., for one isolated cluster. The use of all the available power can be dangerous in terms of the interference caused to other clusters. Due to this, we also consider a different resource allocation.

For the alternative resource allocation, we consider that the available power can be shared among all the APs in the cluster. By doing this, the optimum covariance matrices contain, in the eigenvectors, the optimum precoding matrices without the limitation of the power constraints. These precoding matrices define the optimum power distribution to maximize the data rate. Due to this, we propose to use a scaled version of these covariance matrices, in order to maintain the precoding matrices. More specifically, we solve

$$\begin{aligned} \max_{\{Q_k\}_{k=1}^{\tilde{k}(1)}} \; & \sum_{k=1}^{\tilde{k}(1)} R_k^{\text{DL-2}}(\{Q_i\}_{i=1}^{\tilde{k}(1)}), \\ \text{s.t. } & Q_k \succeq 0, \; k = 1, \ldots, \tilde{k}(1), \\ & \sum_{k=1}^{\tilde{k}(1)} Q_k \leq NP. \end{aligned} \tag{2.17}$$

Let $\{\bar{Q}_k\}_{k=1}^{\tilde{k}(1)}$ be the optimum solution of (2.17). In general, these covariance matrices do not satisfy the individual power constraints in each AP. Due to that, we compute

$$Q_k = \frac{P}{\max_l \left(\sum_{k=1}^{\tilde{k}(1)} \bar{q}_{kl} \right)} \bar{Q}_k, \; k = 1, \ldots, \tilde{k}(1), \tag{2.18}$$

where $\bar{q}_{kl}$ is the l-th element of the main diagonal of $\bar{Q}_k$. The covariance matrices $\{Q_k\}_{k=1}^{\tilde{k}(1)}$ in (2.18) satisfy the power constraints in each AP and, since they are scaled versions of $\{\bar{Q}_k\}_{k=1}^{\tilde{k}(1)}$, they have the same eigenvectors and, hence, they define the same precoding matrices. The optimization problem in (2.17) can be solved with the algorithm presented in [43], or with other techniques that make use of the uplink-downlink duality like in [45] and in [42].

2.6.3 Comparison of solutions for the downlink

In this section, we study the performance of the two previous clustering solutions in the same scenario described in Section 2.5.3, with the same available power at the APs and the same noise power at the receivers. We start showing the achievable sum data rate with different configurations of the UaC solution. Figure 2.11 shows the sum data rate versus the number of UEs for the UaC solution for different values of α, i.e., the maximum number of UEs that each AP

can serve. As it can be observed, the difference between the curves is negligible, even considering cases where the average total power used per AP is very low (see Section 2.6.1). This suggests that the system is limited by interference.

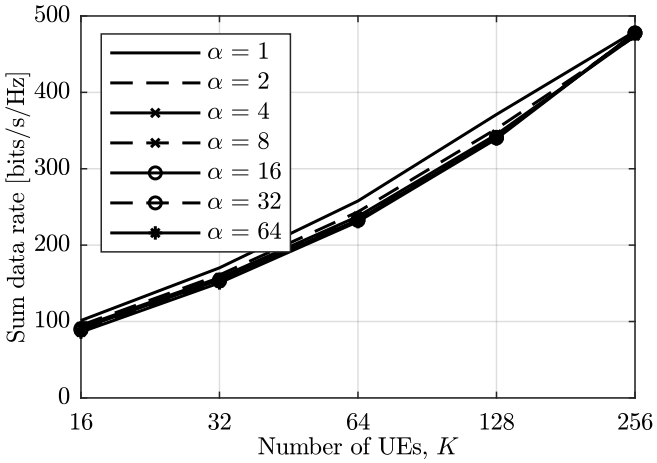

Figure 2.11: Achievable data rate in the downlink for the UaC solution.

Regarding the DC solution, the two power allocation alternatives presented are compared for $N = 16$ and $N = 64$ in Figure 2.12. In the legend, the results corresponding to the suboptimal solution are labelled as "Subopt." while the cluster-optimal power allocation are labelled as "Local opt.". The results highlight that, although the optimal power allocation per cluster (neglecting inter-cluster interference) allows achieving higher per-cluster rate values, the effect of interference makes the total data rates worse than those obtained with the suboptimal power allocation algorithm. In other words, by using all the available power in the APs, the sum data rate is more affected by the interference than benefiting from the increase in transmission power.

Figure 2.13 shows the sum data rate versus the number of UEs for the best case of UaC, i.e. $\alpha = 1$, the DC solution with suboptimal power allocation for cluster sizes (N) equal to 4, 16, 64, 256 y 1024 that coincids with the canonical cell-free massive MIMO solution considering DPC. As it can be noticed, the proposed solution shows a better performance than the UaC solution [39]. Specifically, the performance could improve by 2.5 times for $N = 256$ and 256 UEs in the scenario.

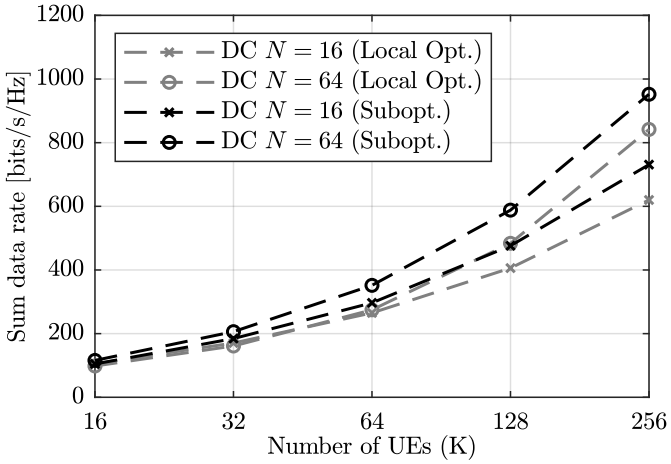

Figure 2.12: Achievable data rate in the downlink for the DC solution.

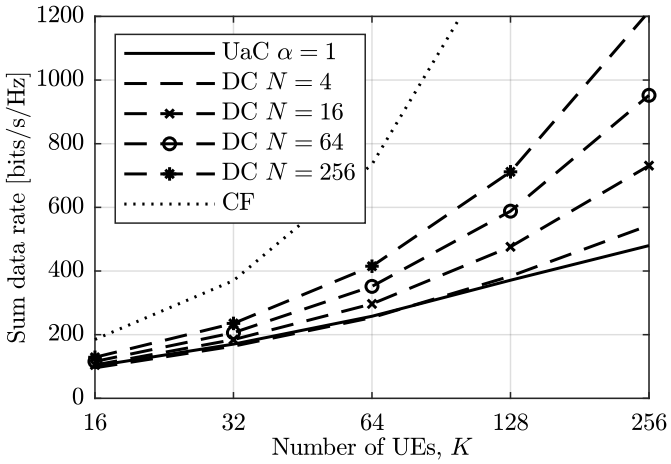

Figure 2.13: Achievable data rate comparison in the downlink.

2.7 Conclusions

The fact that the received power scales without taking into account the antenna orientation or the effective area of the antennas leads to inconsistencies to such an extent that, according to the theoretical model, more power could be received than transmitted. In this chapter, the behavior of the received power and the number of APs where this power is concentrated were analyzed for scenarios of different sizes, taking into account three approaches: $G_r = 1$, considering the radiation pattern of the receiver antennas, and considering the effective area of the receiver antennas. Moreover, it has been concluded that the total received power and the number of APs increase without bound with the scenario size for the first two approaches. Only the approach that considers the effective area has a convergent behavior. This is an important conclusion, especially for the total received power, since, in the real world, the total received power is clearly upper bounded by the transmitted power, a behavior that is only mimicked considering the effective area. As an additional value, with latter solution the receiver antenna gain can be easily integrated in pathloss models.

Additionally, the scalability issues have been studied, considering a definition presented in the literature and its practicality. From this analysis, a new definition of scalability has been proposed. As for how to design a scalable system, several clustering alternatives have been analyzed for both uplink and downlink. In the case of uplink, the best results are achieved neither with clustering techniques that guarantee that the UE is at the center of the cluster nor by creating disjoint clusters that allow interference cancellation, but with a mixed solution. For the downlink case, a disjoint clustering alternative was considered to optimize the resource allocation without losing scalability. Finally, the proposed solution shows a better performance than the state-of-art solution that applies equal power allocation, suggesting that there is room for improvement in the line marked in this Thesis.

Chapter 3

Power consumption modeling in cell-free massive MIMO

The power consumption in massive Multiple-Input Multiple-Output (MIMO) systems [7] has been a concern for the academy community and the industry. This question has been addressed in several publications [18, 22, 23, 46]. The power consumption models of the previously mentioned publications are designed for networks with front-hauls with a dedicated link between the Central Processing Unit (CPU) and each distributed element. However, the front-haul could be shared among multiple Access Points (APs) in serial deployments. For example, as explained in the previous section, a novel technique for cell-free massive MIMO deployment considers the use of radio stripes, a sort of cable with several antenna elements embedded and connected sequentially [47].

In this context, the main contribution of this chapter is to propose some adaptations for the traditional power consumption models to make them valid in downlink for dedicated, serial, and hybrid dedicated/serial front-haul-based deployments. These adaptations consider that the total power consumed in the front-haul does not scale directly with the number of APs connected to the CPU since the front-haul is shared.

A cell-free massive MIMO system, where M APs are deployed, is considered. A CPU connects to all the APs via a front-haul network that consists of N links. Fig. 3.1a shows a generic cell-free massive MIMO deployment.

If $N = M$, each AP will have a dedicated front-haul link (see Fig. 3.1b). Otherwise, if $N < M$, there will be two APs or more serially connected. In the

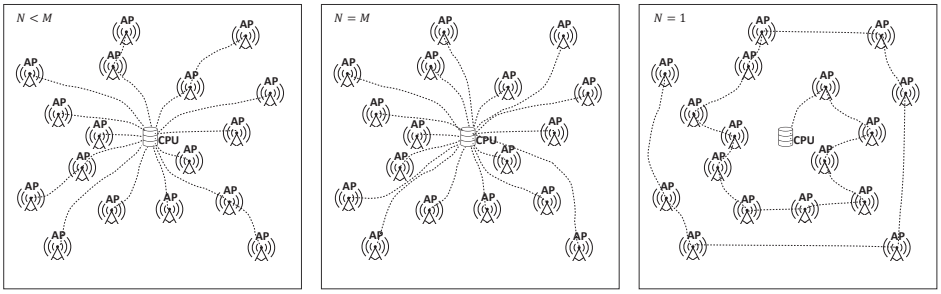

(a) Generic front-haul (b) Dedicated front-haul (c) Serial front-haul

Figure 3.1: Cell-free massive MIMO deployments.

case of $N = 1$, the front-haul is fully serialized (see Fig. 3.1c). Additionally, K users are uniformly distributed in the scenario and served simultaneously.

3.1 Dedicated front-haul

In canonical cell-free massive MIMO systems, the APs are coordinated to serve all users at the same time. Then, it is necessary the exchange of the data of all users and the power coefficients between the CPU and all the APs. Consequently, for dedicated front-hauls, except for the power coefficients, the same information is sent through the N links, where $N = M$.

We are going to focus on downlink transmission. During downlink transmission to describe the power consumption model for a dedicated front-haul deployment. During downlink transmission, the total power consumption depends on the power consumed in front-haul (P_m^{FH} for the m-th link) and the power consumed by each AP (P_m^{AP} for the m-th AP), for both operation and transmission, as explained in the models proposed in [18, 23, 46]. Mathematically, the total power consumption can be expressed with the following set of equations:

$$P_{Total} = \sum_{m=1}^{M} \left(P_m^{FH} + P_m^{AP} \right), \tag{3.1}$$

$$P_m^{FH} = P_m^{FH,fix} + B\chi_m^{FH} S_{dl}, \tag{3.2}$$

$$P_m^{AP} = P_m^{AP,fix} + L_A P_m^{AP,chain} + \frac{(\tau_c - \tau_p)}{\tau_c} \frac{P_m^{tx}}{\alpha_m}, \tag{3.3}$$

In (3.2), $P_m^{FH,fix}$ is the traffic-independent power that is consumed in each front-haul link and depends on the system topology and the distance between

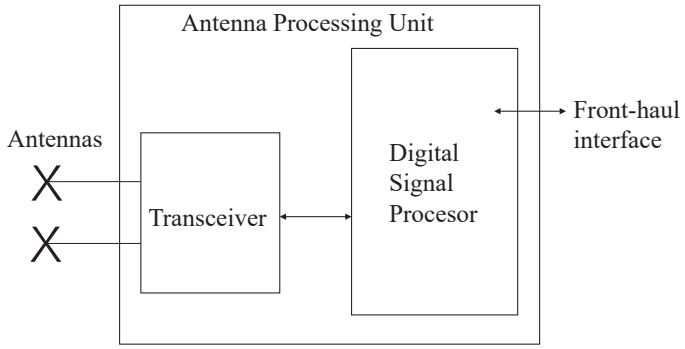

Figure 3.2: Antenna processing unit.

each AP and the CPU [46]. The second term represents the traffic-dependent power, where B is the system bandwidth, χ_m^{FH} is the traffic dependent power consumption coefficient in each link and S_{dl} is the sum spectral efficiency in downlink taking into account all the users. For the sake of simplicity, in this work, P_m^{AP}, $P_m^{FH,fix}$, χ_m^{FH} and in consequence, P_m^{FH} are assumed to be equal for all m.

In order to better understand (3.3), Fig. 3.2 shows the antenna processing unit of each AP consisting of the digital signal processing module, the transceiver and the interfaces to both the antennas and the front-haul. In (3.3), $P_m^{FH,fix}$ is the traffic-independent power that is consumed by, e.g., the site cooling system, the local oscillator and the baseband processors allocated in the digital processing unit [48], L_A is the number of Radio Frequency (RF) chains per AP and $P_m^{AP,chain}$ is the power consumption per RF chain, all of this contained in the transceiver module. Then, the transmitted power and the power used by the amplifier is also added and represented by P_m^{tx}/α_m, where α_m is the power amplifier coefficient. This last term is multiplied by a factor pointing out that the channel estimation is done during the uplink (τ_c is the coherence interval length, τ_p is the training interval length). This estimation can be reused for downlink if Time Division Duplexing (TDD) mode is considered, what it is a common assumption for cell-free massive MIMO systems [7].

It is worth to mention that the P_m^{tx} is much smaller (100-200 mW) than the non-transmitted power (order of Watts), as it is explained in [49]. Due to this issue, focusing on decreasing the consumption of non-transmitted power is important to reduce the total power consumed by the system.

The model discussed above has been used in the context of cell-free massive MIMO in [18, 23, 46] and is based on the model presented for back-haul in [50, 51]. However, in [51], the authors understand the back-haul as set of wireless micro wave links. For obvious reasons, for serial deployments this assumption is no longer valid since for these cases only few or, in the most extreme case, only one link that interconnects all the APs and the CPU is considered.

3.2 Serial front-haul

In this work, we propose some adaptations to adjust the original model presented in Section 3.1 not only to purely dedicated link front-haul but also to hybrid serial/dedicated link front-haul and to fully serial front-haul topologies. In order to express that, a modified total power equation (3.4) is defined considering that for this case, the front-haul power is proportional to the number of serial links (N) instead of M, which supposes a considerable power saving since normally $N \ll M$.

$$P_{Total} = \sum_{n=1}^{N} \left(P_n^{FH,fix} + B\chi_n^{FH} S_{dl} \right) + \sum_{m=1}^{M} P_m^{AP}. \tag{3.4}$$

For the sake of simplicity, in (3.4), it is assumed that $P_n^{FH,fix}$ and χ_n^{FH} are equal for the N links and P_m^{AP} equal for all APs.

As mentioned before, the front-haul technology can also impact on the power consumption. To cite an example, in [52] different embodiments for antennas for distributed massive MIMO are described. These embodiments consider several connection options between the APs and the CPU, additional modules connected to the antenna arrangement and different shapes of the body (cable, strip or film). All of this, definitely affects the network power consumption. A detailed comparison of the power consumption for specific front-haul technologies or multiple lengths of the links is out of the scope of this work. Instead, in Section 3.3, typical values for front-haul power are considered to obtain numerical values for a specific scenario and as a bonus, it is quantified the power saving in terms of fixed power if APs with P_m^{AP} around 1 W are considered.

3.3 Power consumption model comparison

The evaluation scenario consists of an indoor scenario of 50 m $\times$ 50 m, where 100 APs are uniformly deployed with an inter-site distance of 5 m. Addi-

tionally, 20 User Equipments (UEs) are uniformly distributed in the scenario. This configuration is similar to the one proposed in [15], for industrial indoor scenarios.

In order to measure the impact of using dedicated or serial front-haul models, the front-haul power consumption has been estimated, taking into account numerical values from [23] and [46] summarized in Table 3.1. In the case of spectral efficiency in the downlink, the value has been calculated considering an average spectral efficiency per user equal to 4.3 bits/s/Hz as obtained in [15] using max-min fairness power allocation schemes. In the calculations, all the users are considered to be served simultaneously.

Table 3.1: Simulation parameters [15, 23, 46].

Parameters	Value
Power Amplifier efficiency (α_m^{AP})	0.39
AP maximum transmit power (P_m^{tx})	0.1 W
Number of RF chains (L_A)	1
Coherence interval length (τ_c)	200 samples
Training phase length (τ_p)	20 samples
Spectral Efficiency in downlink (S_{dl})	86 Mbits/s/Hz
Bandwidth (B)	20 MHz
Traffic dependent power consumption coefficient (χ_m^{FH}, χ_n^{FH})	0.25 W/Gbps
Fixed front-haul power per link in conventional systems ($P_m^{FH,fix}$)	5 W

3.3.1 Considering conventional APs

In a first study, traditional power consumption values in APs are considered. Specifically, the AP fixed power ($P_m^{AP,fix}$) and the AP fixed power RF chain ($P_m^{AP,chain}$) are assumed to be 8 W and 0.2 W respectively, as in [23].

Figure 3.3 shows the traffic-dependent front-haul power, the fixed front-haul power, the total front-haul power, and the total power versus the number of used serial links using the modified power consumption model. In the graph, the power consumption values associated with fully serial front-haul are allocated at the leftmost point of the curves when $N = 1$ while values associated with fully dedicated front-haul configurations are placed at the rightmost point of the curves. Intermediate values corresponding to hybrid/serial front-haul configurations. As it can be inferred, the rightmost point is equivalent to applying the original power consumption model for a deployment of 100 APs.

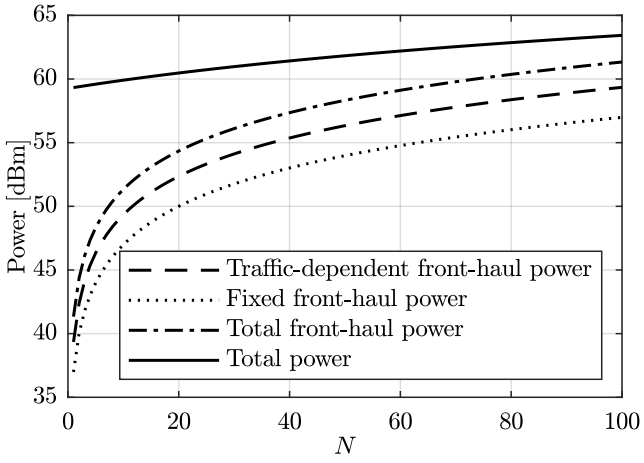

Figure 3.3: Power consumption.

As can be noticed, there is an increasing trend in power consumption concerning using more links to connect the same number of APs. The traffic-dependent and fixed front-haul powers represent 63.24% and 36.76% of the total front-haul power, respectively, independently of the number of front-haul links used. However, if we compare the power consumed in front-haul with respect to total power, we see that the former has a variable impact on the latter depending on how serialized the deployment is. This impact is quantitatively shown in Fig. 3.4.

The graph shows that the total power consumed in front-haul goes from 1.59% for fully serial front-haul to 61.73% for fully dedicated front-haul. As it can be noticed, using the original model would lead to an overestimation of the impact of front-haul power on the total power if serial or hybrid serial/dedicated links were used. In cases similar to this one, our adaptations are vital to obtaining more accurate results.

3.3.2 Considering next-generation APs

In order to assess the impact on the total power consumption of having lower fixed power consumption in the APs, as it is claimed for new generation systems, the front-haul power consumption and transmit power values are kept, while for the power consumed in each AP, the following values are assumed: $P_m^{AP,fix} = 0.75\ W$ and $P_m^{AP,chain} = 0.02\ W$. This way it can be ensured that

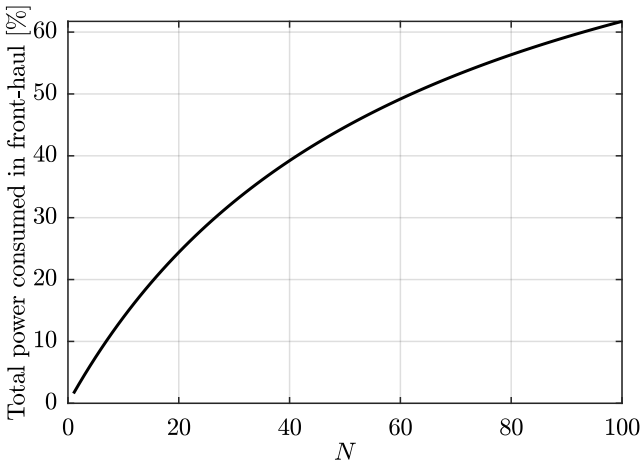

Figure 3.4: Percentage of total power consumed in front-haul considering conventional APs.

the total power consumption in the m-th AP (P_m^{AP}) does not exceed 1 W. It is worth noting that by maintaining the same level of P_m^{tx}, the performance of the communication system is not affected.

In Fig. 3.5, the new total power consumption values are compared with the obtained in Section 3.3.1. As observed, the deployment using next-generation APs has considerable saving power compared to the deployment that uses conventional APs. This power saving, in turn, means that front-haul power has an even more representative impact on total power than what we noted in the previous section. Additionally, for this setup, the front-haul power becomes more relevant, representing 11.96% and 93.15% of the total power for fully serial deployments and fully dedicated deployments, respectively, as shown in Fig. 3.6.

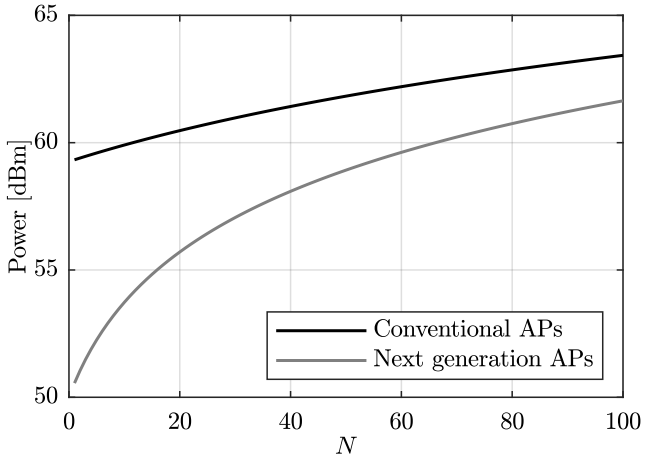

Figure 3.5: Total power consumption comparison.

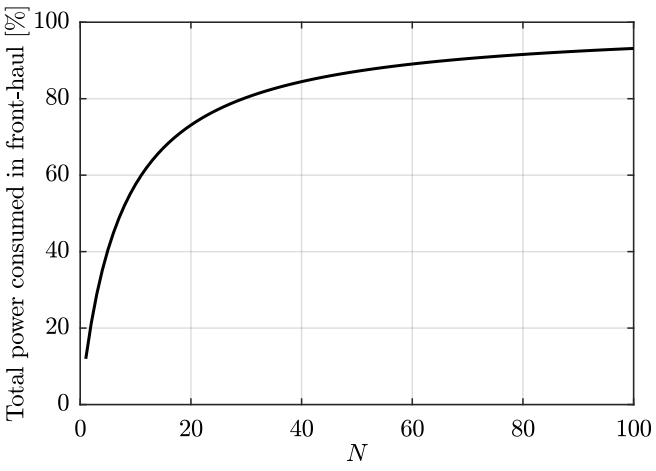

Figure 3.6: Percentage of total power consumed in front-haul considering next-generation APs.

3.4 Conclusions

This chapter has highlighted that traditional power consumption models for distributed systems with dedicated links in the front-haul are not valid when serial links are considered because the consumption would be overestimated in that case. In order to overcome this inconvenience, some adaptations to make the power consumption model valid for serial front-hauls, hybrid serial/dedicated front-hauls, and fully dedicated front-hauls have been proposed.

The role played by the traffic-dependent and fixed front-haul power consumption with respect to the total front-haul power and the total power consumed by the system has been evaluated. According to the results, the fixed front-haul power represents more than three-fifths of the total front-haul power. Additionally, if fully serial and fully dedicated front-hauls are compared, the power consumed in front-haul with respect to the total power can vary considerably from one deployment to another. Finally, when considering next-generation APs and the power savings involved, the power consumed in front-haul becomes an even more significant part of the total power. These facts reinforce the need for using the power consumption model with the proposed modifications to make accurate estimations of the power consumption.

Chapter 4

mmW realistic channel modeling

The channel is the medium through which the transmitted signal propagates from the Transmitter (TX) to the Receiver (RX). Objects and human beings present in the scenario may have less or more influence on the communication channel depending on whether the Line of Sight (LoS) between the TX and the RX is blocked or not. In this context, it is interesting to analyze each of the phenomena involved in signal propagation (Section 4.1). However, there are substantial differences in the electromagnetic properties of the human body with respect to the electromagnetic properties of other objects. This fact motivated the dedication of a section (Section 4.2) to the modeling of body blockage.

In addition, the radio channel is characterized not only by the environment but also by the transmission frequency. In the millimeter Wave (mmW) band, the wavelength, as its name indicates, is in the order of millimeters. This implies that the modeling of the scenarios should be more meticulous because even a small change of surface roughness could greatly impact the channel, specifically in indoor scenarios. In order to generate accurate models for both the scenario and the channel, a powerful simulation tool is presented in Section 4.3. This simulation tool will allow performing a sensitivity analysis to get an idea of how much the details of the scenario, e.g., furniture or building materials, really influence the accuracy of the channel modeling. The related analysis and results are presented in Section 4.4.

4.1 Propagation phenomena

As it propagates in an environment, the signal can experience some amplitude and phase changes depending on the propagation phenomena involved, as shown in Fig. 4.1. If there is LoS, the direct component will be the most powerful and, therefore, the one that will contribute the most to the communication channel, thus minimizing the impact of the other components. If there is Non Line of Sight (NLoS), the components will reach the RX through specular reflections, diffuse reflections, transmission, or diffraction, if applicable.

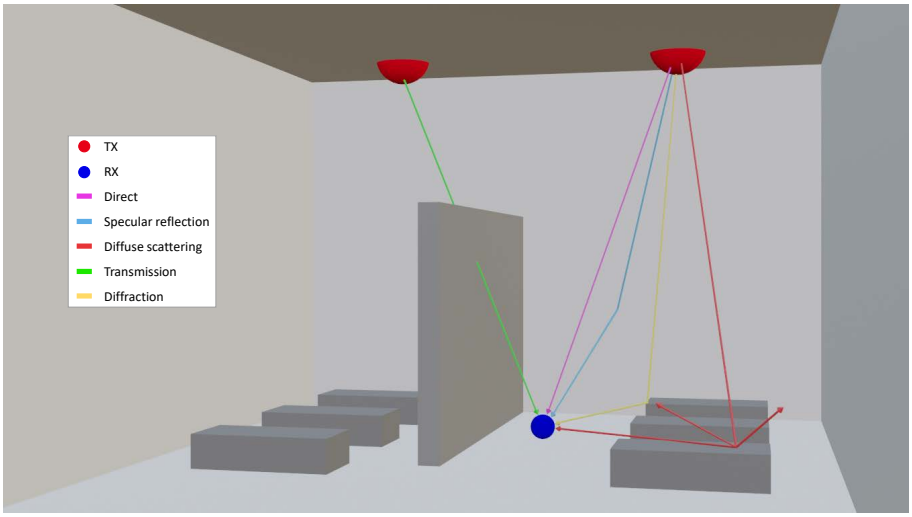

Figure 4.1: Multi-path propagation.

The following is a brief definition of each propagation phenomenon:

- Direct: When the electromagnetic wave follows a direct trajectory from the TX to the RX. In this case, the amplitude and the phase of the signal are only affected by the length of the path between the TX and RX, r, and then the electric field in the far field, E_0, is:

$$E_0 = \frac{\sqrt{30 P_0 D_G(\theta, \phi)}}{r} e^{jk_0 r} \tag{4.1}$$

  where P_0 is the transmission power, $D_G(\theta, \phi)$ is the antenna gain in azimuth and elevation and $k_0 = 2\pi/\lambda$ is the wave constant in free space.

- Specular reflection: When the signal impacts a polished surface and is redirected in a single direction. The electric field of the reflected beam for a given incident angle ψ is

$$E = r_x \frac{e^{-\frac{j2\pi fd}{c}}}{d}, \tag{4.2}$$

where r_x would be r_h for the horizontal polarization and r_v for the vertical polarization, and d is the path length for the reflected ray (from the TX to the reflection point and from there to the RX). The Fresnel reflection coefficients are

$$r_h = \frac{\sin\psi - \sqrt{\varepsilon^* - cos^2\psi}}{\sin\psi + \sqrt{\varepsilon^* - cos^2\psi}}, \tag{4.3}$$

$$r_v = \frac{\varepsilon^* \sin\psi - \sqrt{\varepsilon^* - cos^2\psi}}{\varepsilon^* \sin\psi + \sqrt{\varepsilon^* - cos^2\psi}}, \tag{4.4}$$

where ε^* is the complex relative permitivity.

- Diffuse scattering: When the wave impacts a rough surface and is redirected in several directions. In this case, for the computation of the electric field there are two main approaches. One, the directive model, considers that the energy is scattered in the directions around reflection angles. The other, the Lambertian model, considers that the energy is scattered in all directions centered in the norm of the point where the diffuse scattering occurs. More details of the diffusse scattering modeling could be found in [53].

- Transmission: When a part of the signal penetrates through the surface and is transmitted beyond it. The electric field of the transmitted beam for a given incident angle ψ is

$$E = t_x \frac{e^{-\frac{j2\pi fd}{c}}}{d}, \tag{4.5}$$

where t_x would be t_h for the horizontal polarization and t_v for the vertical polarization, and d is the path length in meters for the transmitted ray (from the TX to the impact point and from there to the RX). The Fresnel coefficients for transmission are

$$t_h = \frac{2\sin\psi}{\sin\psi + \sqrt{\varepsilon^* - cos^2\psi}}, \tag{4.6}$$

$$t_v = \frac{2\sqrt{\varepsilon^*}\sin\psi}{\varepsilon^* \sin\psi + \sqrt{\varepsilon^* - cos^2\psi}}. \tag{4.7}$$

- Diffraction: When the wave circumvents the object, which becomes a second source of energy. This phenomenon is modeled using the Geometrical Optics algorithms and the Uniform Theory of Diffraction that allow to find the diffraction coefficients. Then, based on these coefficients, the electric field is computed. More details of the diffraction modeling could be found in [53].

As can be deduced from the definitions, the frequency of occurrence of each of these phenomena will depend on the particular scenario and the network deployment designed for it. For example, suppose the scenario under study is an open plant, and a distributed antenna deployment is performed. In that case, the probability of having LoS at any point in the scenario is high; therefore, the contributions due to other propagation phenomena will have less influence. In other scenarios, such as offices, where people are moving around, and the TX could hypothetically be placed in the central area of the ceiling, the LoS may occasionally be blocked by the human body. In that case, the signal could reach the RX by reflecting on the desks, chairs, etc., or by circumventing the objects or the human body itself.

4.2 Body blockage modeling in mmW

The blockage effect at the mmW band has been a reason of concern due to the difficulty of transmitting effectively in NLoS conditions at these frequencies. One of the elements that block the mmW signals is the human body. In fact, it can be the most critical blocker in open-space indoor environments, typically with high human density. Indeed, it is essential to model each blocker accurately and consider the presence of multiple blockers appropriately. For example, in [54], Jacob *et al.* presented an extension of the Ray Tracing (RT)-based stochastic human blockage model for the IEEE 802.11ad standard at 60 GHz, which considers the presence of up to 10 users. In contrast, the original model only considered one user. The estimations of the model are more realistic in, e.g., conference rooms.

Given this importance, a part of the research community has been recently focused on improving the human blockage models to get more realistic results. In [25], a human-body blockage model based on the Double Knife-Edge Diffraction (DKED) is presented. This model offers a simple numerical representation for calculating the body blockage losses. Moreover, the Third Generation Partnership Project (3GPP) has incorporated the research conducted in this field to define blockage modeling as an add-on feature to the channel model in [55]. This channel model is used in the 3GPP evaluations of the physical

layer in the 0.5-100 GHz frequency range. The body blockage model considers two variants: one based on a stochastic method and the other based on a geometric method. The first model (Model A) can be used in cases where generic modeling is enough to capture human and vehicular blocking. Due to its simplicity, this model does not demand a high computational cost. The second model (Model B), inspired by the model presented in [25], was designed for those cases where more realistic modeling of the scenario and the blockers is needed. Nevertheless, the computational complexity of this model is still much lower than in the case of a RT approach [56], where several rays need to be launched to mimic the signal propagation in real life. In Model B, the human bodies in a scenario are considered blockers of a link between a TX and a RX based on a proximity criterion. Specifically, only those close to the RX are considered blockers. Then, the blockers are modeled as rectangular screens with one diffraction point per edge, positioned in the middle of each side, and their contributions are calculated in an isolated manner. Finally, the contributions from each blocker are summed.

Additionally, the Mobile and wireless communications Enablers for Twenty-twenty Information Society (METIS)/3GPP model has been studied, e.g., in [57]. This work proposed an adaptation of the model that takes into account the use of directional antennas.

Taking into account the progress made so far in the development of models that consider the human body, in [58], proposed some adaptations for improving the accuracy of the 3GPP body blockage model. These proposals are detailed below, as well as their validation through comparison with real measurements and the results obtained with the original 3GPP body blockage model.

4.2.1 Proposals for 3GPP Body Blockage Model Improvement

Re-position of the Diffraction Points

In the 3GPP blockage model, the human blockers are modeled as rectangular screens whose normal vectors are parallel to the floor and oriented towards the TX. The infinite set of real diffraction points around the object are then discretized, for the sake of simplicity, leaving a central one at each edge of the screen (see in Fig. 4.2, point D).

This model is totally valid when omnidirectional antennas are considered or, in general, when a signal beam coming from a TX antenna hits the blocker in its full amplitude. However, cases where this beam does not cover the entire screen may occur, especially when working with directional antennas at a relatively short distance. In such cases, calculating the diffraction points based on the

location of the antennas and the beam pointing would be more accurate. In fact, we propose to take as diffraction points those lateral points that are at the height where the central components of the beam emitted from the TX antenna are impacting (see in Fig. 4.2, point D').

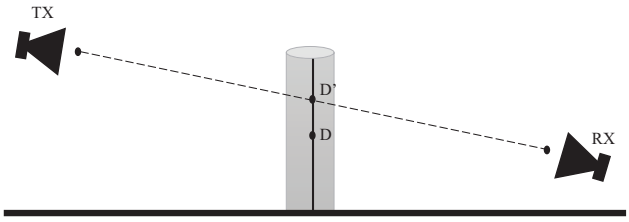

Figure 4.2: Re-position of diffraction points (side view).

Blockage Area Determination

In order to apply the 3GPP body blockage model in a scenario for a specific TX - RX link, the first step is to determine which elements of the scenario are considered as blockers. The criterion from the 3GPP is to consider as blockers those elements which are "close" or at a "certain distance" from the RX. The drawback of this criterion is evident, as it does not provide an objective criterion to be followed in every situation. In addition, this criterion may be valid in scenarios with high-height TX antennas. Still, if the TX antenna height is low, a human close to the TX may also block the signal directed towards a distant RX. The latter may be the case for scenarios where device-device communications are considered. To provide a more precise determination, valid also in scenarios with low-height antennas, we propose to use the concept and calculation procedure of the blockage zone presented in [59]. In that paper, the blockage zone concept is used as a criterion to determine if a moving object is blocking the radio signal to be able to model the system capacity in a random field of moving potential blockers. The contribution of this Thesis is to use this concept integrated with the 3GPP channel model.

For the sake of completeness, we explain the blockage area concept in the following lines. Given a specific location and height of a TX and an RX, and a specific combination of width and height for potential blockers, in [59] the blockage area is defined as a region around the RX where any potential blocker would be effectively blocking the LoS from the TX. The concept is illustrated in Fig. 4.3. A blockage area is shown as a shaded area between the TX and the RX. Two potential blockers are shown as cylinders. The cylinder whose axis falls within the blockage area is considered as a blocker, while the other whose

axis is out of the blockage area is not considered as blocker. We propose to use a simplified rectangular shape for the blockage area, as shown in Fig. 4.3, following the approach of [59]. Specifically, given a body width, the blockage area can be modeled as a rectangular region of *body width* x $R_{blockage}$ squared meters, where $R_{blockage}$ can be calculated with the following equation:

$$R_{blockage} = \begin{cases} d_{TX'-RX'} \left(\frac{h_{body} - h_{RX}}{h_{TX} - h_{RX}} \right) & \text{if } h_{TX} > h_{RX} \\ d_{TX'-RX'} & \text{if } h_{TX} = h_{RX} \end{cases} \tag{4.8}$$

where TX' and RX' are the projections of TX and RX onto the floor plane, $d_{TX'-RX'}$ is the distance between TX' and RX', and h_{TX}, h_{RX} and h_{body} are the heights of the TX, RX and blocker, respectively (see Fig. 4.3). Cases where the TX height is less than the RX height are not considered.

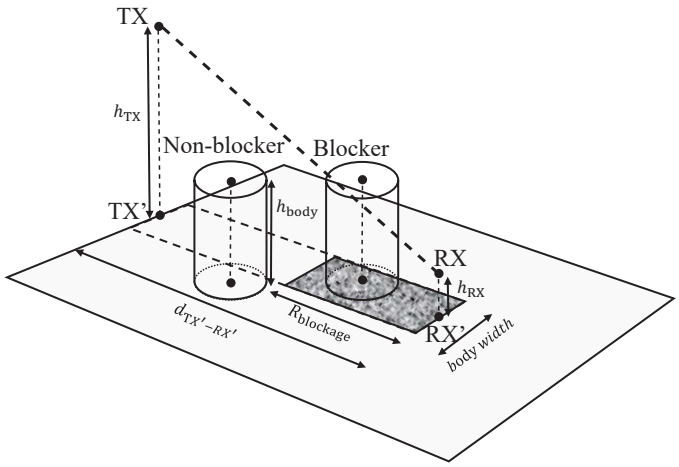

Figure 4.3: Blockage area determination.

Close Blockers Grouping

When multiple blockers are considered, it may be the case where the link from the diffraction points of some of them to the RX is also blocked by other blockers. In that case, the blocking losses may be higher than the values provided by the 3GPP because, in its model, the contributions are calculated separately for each blocker and summed.

This Thesis focuses on a specific case in which various blockers are so close that they are perceived as a single body of greater width. What is proposed in that case is to include them in the 3GPP model as a body K times wider, being

K the number of blockers close to each other. Two bodies can be modeled as a single body if the cylinders modeling them overlap or are, at least, side by side (see Fig. 4.4).

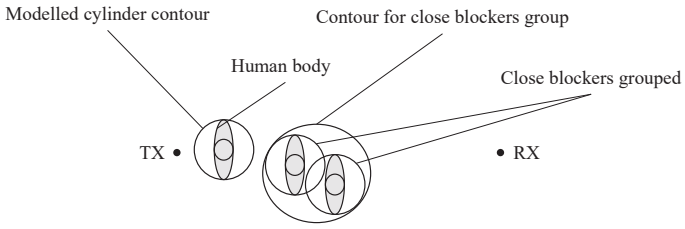

Figure 4.4: Grouping of close blockers.

4.2.2 Scenario and Setup for Measurements

Scenario

The measurement scenario is an indoor open space. The distance between the TX and the RX is 4 m, and their height is 1.2 m, similarly to previous works [57, 60]. Fig. 4.5 illustrates this scenario. The measurements were carried out for one, two, and three human blockers. For the case of one blocker only (Case 1), this one was positioned facing the RX antenna, over the TX'-RX' line, at 7-different locations going from 0.5 m to 3.5 m from the TX with steps of 0.5 m. For Case 2 and Case 3, two and three humans, respectively, were positioned side by side with the same orientation and locations considered in Case 1. In Case 2, the two humans are positioned as close as possible, and the edge between the bodies is over the TX'-RX' line. In Case 3, the middle blocker is over that TX'-RX' line. Cases 2.1 and 3.1 are modifications of Case 2 and Case 3. In both cases, a blocker is in the same location as the single blocker of Case 1. The second blocker is positioned just after the first blocker with a half-body shift from the TX'-RX' line. Whereas, in Case 3.1, the third blocker is also positioned after the first blocker but presents half body shift from the TX'-RX' line in the opposite direction of the second blocker shift. The measurements are repeated for all cases, alternating the participants, to obtain consistent results. Table 4.1 presents the three volunteers' physical characteristics and participation in each measurement case. For each specific measurement, the measurement duration is 4 seconds, generating 100,000 samples from which we obtain the median value.

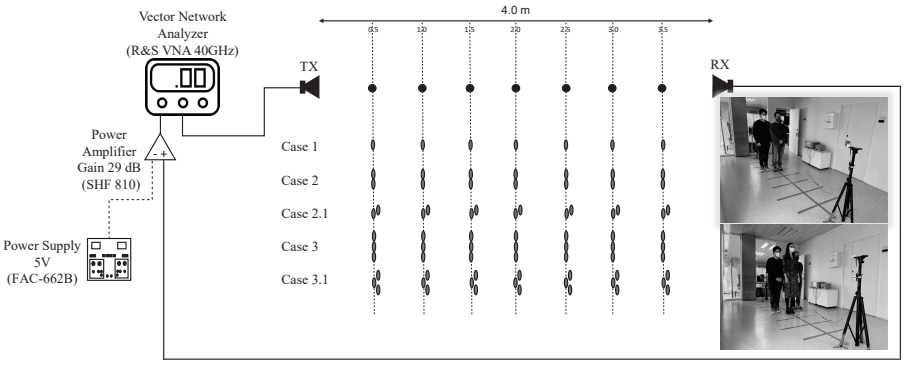

Figure 4.5: Setup and measurement cases. Case 2.1 (upper picture), Case 3.1 (lower picture).

Table 4.1: Volunteer information.

Id	Breadth [m]	Depth [m]	Height [m]	Case involvement
1	0.39	0.21	1.81	Case 1, 3, 3.1
2	0.43	0.24	1.70	Case 2, 2.1, 3, 3.1
3	0.42	0.25	1.73	Case 2, 2.1, 3, 3.1

Setup

Fig. 4.5 illustrates the measurement setup used in this assessment to obtain body blockage losses measurements at 30 GHz with 50 MHz of bandwidth signal. A Vector Network Analyzer (VNA) measures the losses between the transmitted and the received signals. The TX antenna is connected to port 1 of the VNA, and an amplifier is connected between port 2 and the RX antenna. The VNA is the ZNB40 of the manufacturer Rhode&Schwarz, with a working frequency range between 100 MHz and 40 GHz. The output power is fixed to 0 dBm in our measurements. The amplifier is an SHF 810 with a gain of 29 dB. The antennas are identical WRD180 wideband horn antennas, with 14.1 dBi of maximum gain and a 3-dB beamwidth of 30 degrees at 30 GHz [61]. According to the antenna characteristics and the working frequency, the far field distance is approximately 0.25 m, so it can be assured that the signal is received in the far field for all cases considered in this work.

4.2.3 Results and Analysis

This section compares the measurement results obtained in the scenario presented in the previous section with the predictions of the 3GPP human body blockage model with and without our proposed modifications related to the positioning of the diffraction points and the modeling of close blockers. In all the cases, the 3GPP model was extended following the approach in [57] to considering directional antennas. Therefore, the technical specifications of the antennas used in our measurements were considered in calculating losses. Specifically, the half power beamwidth of the antennas involved has been used in the equation 5 from [57] to obtain the parameters a and b. The gain of antennas has been computed and finally used in the equation 6 from [57] to determine the body blockage losses.

Concerning the criterion to determine which bodies are signal blockers, following the blockage area determination method explained in Section 4.2.1, all the human bodies involved in the measurements should be considered blockers except the two side bodies in Case 3. The reason is that given that the heights of the TX and RX are equal, the blockage area extends from the TX to the RX, as shown in Fig. 4.6. Therefore, all the potential blockers can effectively block the signal irrespective of their distance to the TX or RX, contrary to what is stated by the 3GPP model. On the other hand, the width of the blockage area is equal to the width of a potential blocker. As a result, the side bodies in Case 3 are out of this region and should not be considered effective blockers.

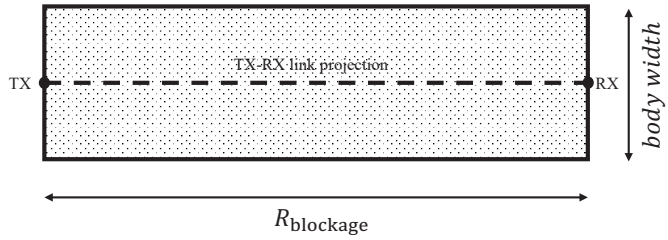

Figure 4.6: Zenithal view of the blockage area in our measurement setup.

In the 3GPP blockage model, the human blockers are modeled as rectangular screens with a height of 1.7 m with its standard vector parallel to the floor and oriented towards the TX. The diffraction points on the left and right sides of the screen are located in the middle of the side edge, i.e., at the height of 0.85 m. In our setup, the TX and RX antennas are positioned at the height of 1.2 m. Therefore, the TX-RX line-of-sight cuts the screen at the height of 1.2 m. In order to analyze the impact of the precise position of the diffraction points, the loss predicted by the 3GPP model is compared with side diffraction

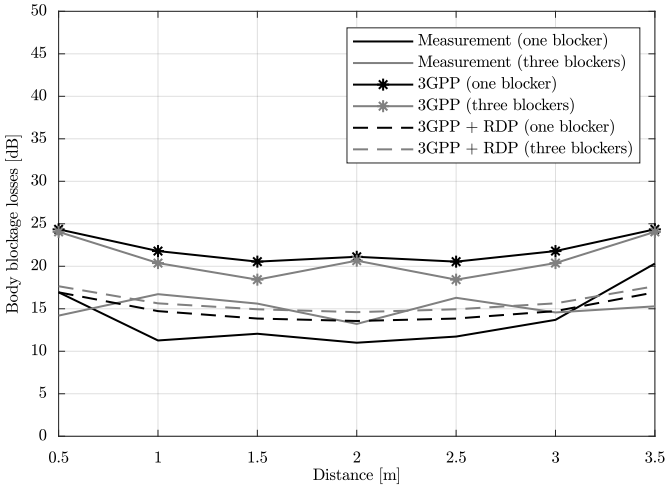

Figure 4.7: Body blockage losses: Case 1 (one blocker) and Case 3 (three blockers in parallel).

points at 0.85 m, as in the original model, and at 1.2 m, as proposed in Section 4.2.1, with the results of actual measurements considering a single blocker, i.e., focusing on the Case 1 explained in the previous section.

The results are shown in Fig. 4.7, where the body blockage losses for Case 1 and Case 3 are represented as a function of the distance from the blockers to the RX. The actual measurements for one blocker are denoted as "Measurement (one blocker)", the 3GPP model without modifications as "3GPP (one blocker)", and the 3GPP model with the re-positioning of diffraction points (RDP) as "3GPP+RDP (one blocker)". The mean absolute error for the 3GPP model is 8.21 dB, while the error is 2.05 dB with the proposed modification. This result reinforces this approach. In Case 3, applying the method proposed in this work to determine which human bodies should be considered as blockers leads to considering only one blocker, concretely, the central human body. For the sake of comparison, measurements with the Case 3 setup are included ("Measurement (three blockers)") as well as the results when the three bodies are considered blockers as "3GPP (three blockers)" for the original model (with the original diffraction points) and "3GPP + RDP (three blockers)" for the 3GPP model with the re-position of diffraction points. Results demonstrate the validity of the proposed approach to determine the bodies that should be considered blockers and corroborate the increased accuracy provided by the discussed positioning of the diffraction points.

In Case 2, Case 2.1, and Case 3.1, the application of the criterion proposed in this work to determine the blockers leads to more than one blocker being considered. Therefore, in these cases, the validity of the proposal for close blockers grouping (CBG) presented in Section 4.2.1 was analyzed. The results of the measurements and the model calculations are shown in Fig. 4.8, Fig. ,4.9 and Fig. 4.10, respectively. As in the previous cases, it is depicted the result of the measurements ("Measurement"); the original 3GPP model ("3GPP") with an absolute error concerning measurements of 27.77 dB for Case 2, 20.16 dB for Case 2.1, and 4.03 dB for Case 3.1; the result of modifying the diffraction points location ("3GPP + RDP") with an absolute error of 4.17 dB for Case 2, 3.53 dB for Case 2.1 and 7.85 dB for Case 3.1; and the result of also grouping closely spaced bodies ("3GPP + RDP + CBG") with an absolute error of 6.34 dB for Case 2, 4.03 dB for Case 2.1 and 2.98 dB for Case 3.1. Considering that, generally, the results of "3GPP + RDP" are optimistic. The results of "3GPP + RDP + CBG" are pessimistic. An additional graph ("avg(3GPP + RDP, 3GPP + RDP + CBG)") has also been included presenting the average result of the two last approaches, i.e., the average losses of the cases with grouping and without grouping of blockers. This is precisely the approach that provides the most accurate results in all the cases (absolute error equal to 1.28 dB, 3.62 dB, and 2.84 dB for Case 2, Case 2.1, and Case 3.1, respectively) and the one we propose to be followed in case of having close blockers in a scenario.

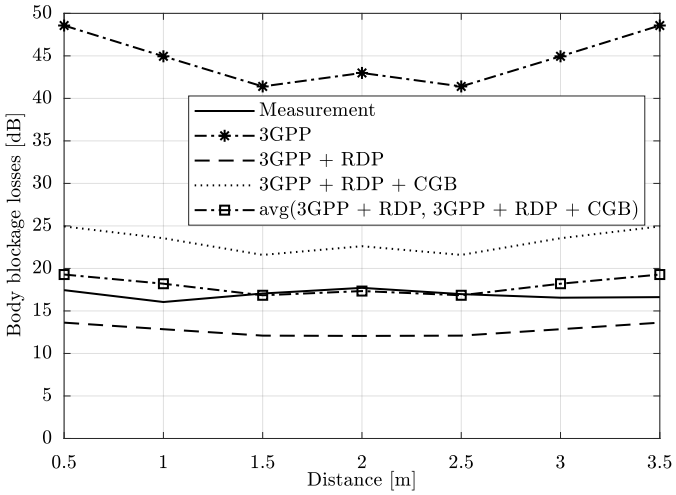

Figure 4.8: Body blockage losses: Case 2.

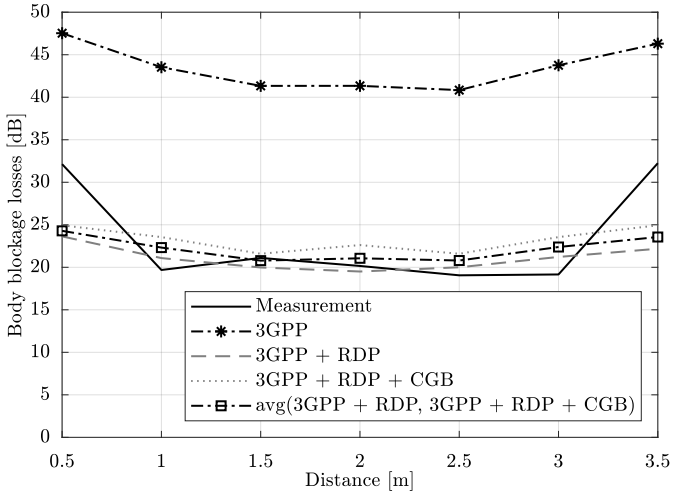

Figure 4.9: Body blockage losses: Case 2.1.

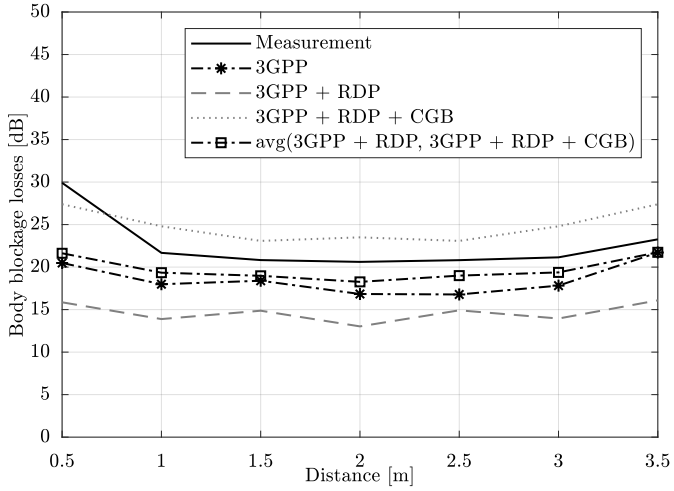

Figure 4.10: Body blockage losses: Case 3.1.

As demonstrated, more accurate results can be achieved with the modifications proposed while keeping simplicity.

4.3 Realistic modeling and simulation

Statistical channel models are based on probability density functions of the transmission parameters that define each environment. WINNER II [62], IMT-Advanced, [38] and 3GPP-3D [63] are among the most important statistical propagation models. However, at the mmW band and especially for indoor scenarios, the stochastic models could not be able to consider all the relevant details. In these circumstances, the deterministic models are more suitable. The latter can reproduce the channel based on reliable knowledge of the geometric and electromagnetic features of the scenario.

Regarding deterministic channel modeling, the most common technique is the RT. Several channel simulators have been developed based on them [64–68]. Moreover, the iTEAM has designed its channel modeling tool based on RT and developed it over the Unity 3D platform [69]. This platform is a video game engine that facilitates realistic scenario modeling. In addition to this advantage, it also has raycasting and scripting tools that enable the modeling of RT techniques, the electromagnetic characterization of the scenario, and channel modeling. The novel tool has been tested for both indoor and outdoor scenarios and, besides, for vehicle-to-vehicle communications [70, 71].

Additionally, given the spectral closeness between the visible spectrum and the mmW bands, it has been proposed the use of light propagation modelling tools for radio channel modelling [72]. This tool has also been developed over the Unity 3D platform, taking advantage of its friendly interface and the advanced RT algorithms of the lighting processes performed by the game engines.

In this section, the Unity 3D features that make possible the modeling of the physical and electromagnetic characteristics of the objects are described. Moreover, it is explained in detail what the RT techniques consists of, and some basics of its implementation over Unity 3D. Additionally, the Light Intensity Model (LIM) is presented as an alternative to traditional RT algorithms and some insight into its capabilities and the results that have been achieved to this point, are provided.

4.3.1 Scenario modeling

The importance of realistic modeling in mmW for accurate channel modeling has been commented previously. Nowadays there are several tools that make it possible to design realistic scenarios or reproduce real scenarios with great precision such as Blender, Autodesk Maya, Unreal Engine, Unity 3D, among others. For this Thesis the realistic modeling of the scenarios has been carried out in Unity 3D.

In Unity 3D, it is possible to create a scene and then start to add all the objects that should be present conveniently. In order to do this, Unity provides 3D primitive objects such as cubes, spheres, capsules, and cylinders. However, it is also possible to import complex models with a high level of detail from external applications, e.g., SketchUp, Blender, and ProBuilder. Additionally, each scene object has properties such as position, rotation, scale, layer, material, etc. An example of the outdoor scenario generated with complex 3D objects such as trees, multi-story buildings and streets, is shown in Fig. 4.11.

Figure 4.11: Realistic outdoor scenario.

Unity 3D also provides 2D objects that play a relevant role in the visualization and the interactivity with the simulation tools. These 2D objects could be as simple as a triangle or as sophisticated as a button. Figure 4.12 is a screenshot of the planning tool developed at iTEAM, where a menu is shown. Through this menu it is possible select different use cases to be studied by clicking on the correspondent button.

Figure 4.12: Visualization and interactive menu.

4.3.2 Channel modeling

RT technique is based on deterministic modeling and is appropriate for predicting channel fluctuations. This has been used for decades [73]. The technique consists of launching rays from a TX and analyzing the scenario's impact on them. The presence of objects or structures in the scenario modifies the trajectory and the strength of the rays according to the electromagnetic properties of these objects and structures. The channel model is based on all the changes in phase and amplitude suffered by the rays.

Implementing the techniques in Unity 3D is based on a function called Raycast. This function consists of casting a ray against all objects in the scene and allows to know whether an object has been intersected or not. Once the intersected objects have been identified, their materials and their electromagnetic characteristics are also detected. This step directly impacts the direction and amplitude of the rays cast later, having the previous impact point as the origin.

Additionally, for the channel modeling, it is important to assign electromagnetic properties to the objects of the scene depending of the materials they are made of and following Table 4.2. In the referenced work, the equations to calculate the permittivity and conductivity from the parameters shown in the table are also provided. The calculation of the real part of the relative permittivity (ε'), the imaginary part of the relative permittivity(ε''), and the

conductivity (σ) are given by

$$\varepsilon' = a \cdot f^b, \tag{4.9}$$

$$\varepsilon'' = 17.98\frac{\sigma}{f}, \tag{4.10}$$

$$\sigma = c \cdot f^d, \tag{4.11}$$

where f is the frequency in GHz and c is the speed of light in a vacuum.

Table 4.2: Material electric parameters [74].

Material	**Permitivity**		**Conductivity**		**Frequency**
	a	**b**	**c**	**d**	**GHz**
Vacuum ($\approx$ air)	1	0	0	0	0.001-100
Concrete	5.31	0	0.0326	0.8095	1-100
Brick	3.75	0	0.038	0.8095	1-100
Plasterboard	2.94	0	0.0116	0.7076	1-100
Wood	1.99	0	0.0047	1.0718	0.001-100
Glass	6.27	0	0.0043	1.0718	0.1-100
Ceiling board	1.50	0	0.0005	1.1634	1-100
Chipboard	2.58	0	0.0217	0.7800	1-100
Floorboard	3.66	0	0.0044	1.3515	50-100
Metal	1	0	10^7	0	1-100

At this point, the propagation phenomena models discussed in Section 4.1 should by applied depending on the ray trajectory from the TX to the RX and the electromagnetic properties of the materials.

Figure 4.13 is a screenshot a the UPV planning tool where a realistic indoor scenario appears. Using the simulator capabilities, it is possible to assign locations for the TX and the RX, and then, through the RT-based computation, determine the pathloss between the two points. The figure shows the paths that connects the TX and RX, being the magenta ray the direct path and the yellow rays, the reflected paths. As can be seen in the menu in the left, the pathloss for in this case is 79 dB.

Despite the accuracy that characterizes RT based modeling, in some cases, its computational cost makes it unfeasible. Faced with this drawback, a LIM [72] has been presented for mmW, which is based on the electromagnetic similarities between mmW and light. Concerning the lighting processes, games engines have specific tools for those tasks. For example, Unity has the Global

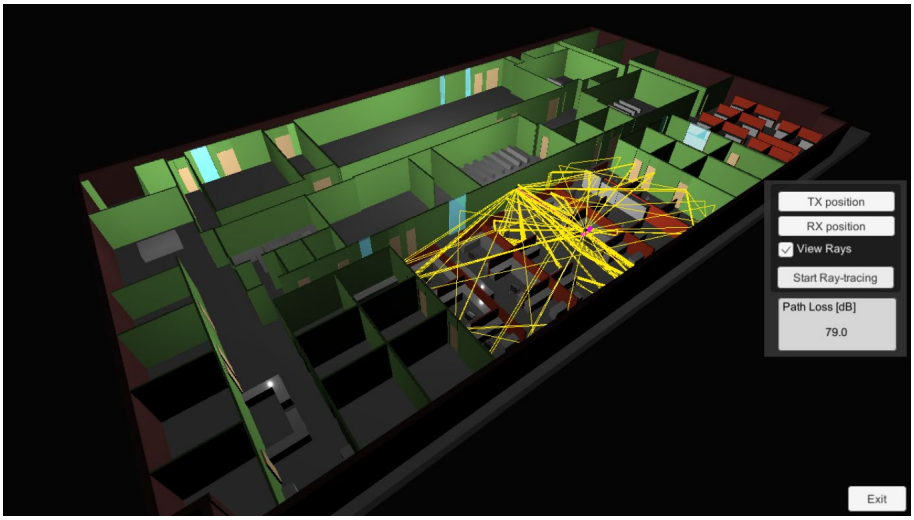

Figure 4.13: Ray-tracing simulation.

Illumination (GI) advanced lighting tool. The GI is a group of algorithms and mathematical models that attempts to simulate the complex behavior of light, i.e., specular reflections, diffuse reflections, refractions and each one of the phenomena associated with the propagation of light. Another relevant feature of Unity is that it is possible to modify the configuration of the materials of the Three Dimensions (3D) objects to have an interaction with the light closer to the interaction of those materials with the radio waves. In the case of our LIM implementation, the texture of the materials is adjusted with that aim. Specifically, extremely smooth materials can emulate high reflective materials such as metal while different levels of roughness could be assigned to materials originating diffuse scattering.

4.4 Sensitivity analysis of the modeling realism

As mentioned above, it is foreseeable that in the mmW band, the characterization of the scenario, especially if it is indoor, will play a fundamental role. It is therefore considered appropriate to carry out a study to quantify the effect of a more or less accurate scenario modeling on the radio channel. In particular, this section proposes a sensitivity analysis of modeling realism. First, some insights about channel modeling are introduced. Then, the scenario is presented. Finally, simulation results for different accuracy levels in the scenario modeling are compared with real measurements.

4.4.1 Presentation of the scenario

The scenario selected for the study is described in [75]. This selection was motivated by the fact that this scenario is widely documented in the literature and the availability of measurement data. The scenario is located on the 9th floor of a 10-story building built in the 1990s with tinted windows and steel reinforcement between each floor. The scenario comprises spaces such as common cubicle offices, lecture rooms, and corridors. The most common scenario materials are concrete, drywall, metal, and chipboard.

In [75], a total of 5 and 33 locations were selected for the TX and RX measurements, respectively, resulting in measurements from 48 TX-RX location combinations and considering LoS and NLoS propagation conditions. However, for the purpose of this study, only positions 1 of the TX and positions 1 to 8 of the RX have been selected. By focusing on these TX-RX combinations, it is possible to evaluate the propagation under different circumstances, e.g., LoS/NLoS in an open space or in a corridor. These cases will be analyzed in detail in Section 4.4.3.

Using the iTEAM planning tool, the real indoor scenario has been modeled as shown in Fig. 4.14. The materials are highlighted in different colors in the figure, and the TX and RX positions are also marked. The materials characterized are concrete (red), plasterboard (green), metal (orange), glass (blue), and chipboard (gray and yellow). At the same time, the selected TX and RX positions are labeled in green and purple, respectively.

4.4.2 Different accuracy levels in the scenario modeling

In order to quantify the impact of the furniture and materials on the propagation for the presented indoor scenario, different scenario configurations are proposed. The fourth scenario configurations proposed are as follows:

- **Calibrated scenario (Configuration 1):** All the furniture and the materials are as considered in the original scenario.

- **Unfurnished scenario (Configuration 2):** The scenario consists only of the physical space itself and the transmitting and receiving antennas. No furniture is considered.

- **Rough material characterization (all concrete) (Configuration 3):** The scenario is unfurnished, and the electromagnetic characteristics of the building materials are not properly considered. Specifically, all the materials in the room are characterized as concrete.

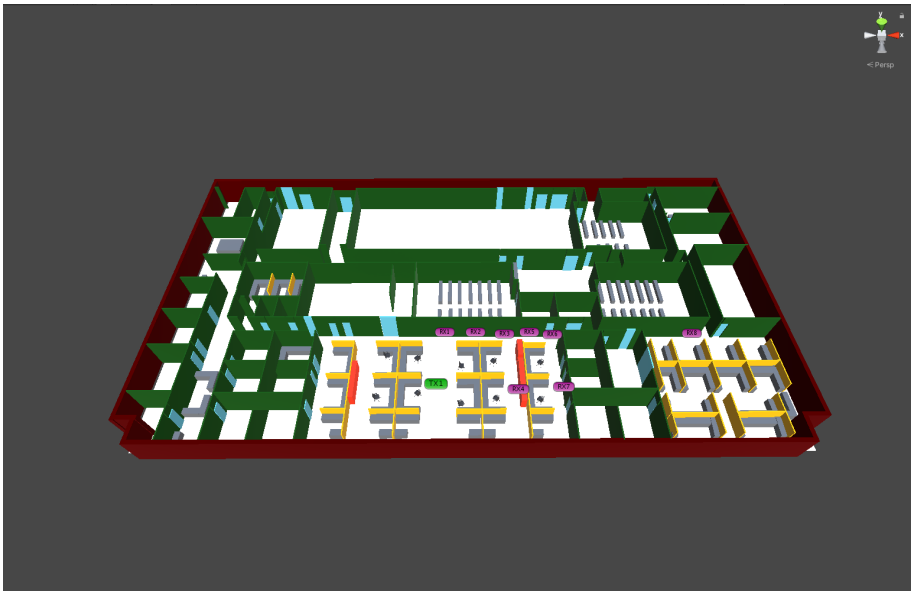

Figure 4.14: 3D scenario developed in Unity3D and TX-RX location.

- **Rough material characterization (all plasterboard) (Configuration 4):** The scenario is unfurnished, and the electromagnetic characteristics of the building materials are not properly considered. Specifically, all the materials in the room are characterized as plasterboard.

4.4.3 Analysis and numerical results

Table 4.3 shows the LoS condition and the pathloss at 28 GHz with co-polarized antennas for every couple of TX-RX for the configurations described in the previous section. For the sake of comparison, the data are also represented in Fig. 4.15.

In Fig. 4.15, the measurement results taken from [75] are drawn with a solid black line, while the simulation results considering the different configurations of the scenario are shown in gray with different line patterns. From the first glance, it can be seen that the results obtained with the calibrated scenario match the measured values very well. However, everything is not black and white, i.e., for some RX positions, values similar to the measured values are obtained regardless of the configuration, and for others they are only achieved if the scenario is calibrated. For example, at the RX 1 position, it can be seen that all curves are close to the real value, being the most significant difference

Table 4.3: Pathloss values.

LoS condition	TX ID	RX ID	Meas. (dB)	Conf. 1 (dB)	Conf. 2 (dB)	Conf. 3 (dB)	Conf. 4 (dB)
LoS	1	1	69.3	68.6	67.5	67.4	69.1
LoS	1	4	75.3	75.6	78.4	78.9	78.1
LoS	1	7	76.5	75.6	82.5	80.0	82.2
NLoS	1	2	76.6	77.0	82.1	80.5	82.0
NLoS	1	3	82.7	84.0	81.7	79.5	80.2
NLoS	1	5	84.3	84.0	80.1	78.7	81.4
NLoS	1	6	86.4	86.1	88.2	87.7	90.0
NLoS	1	8	95.9	97.4	98.3	93.7	98.3

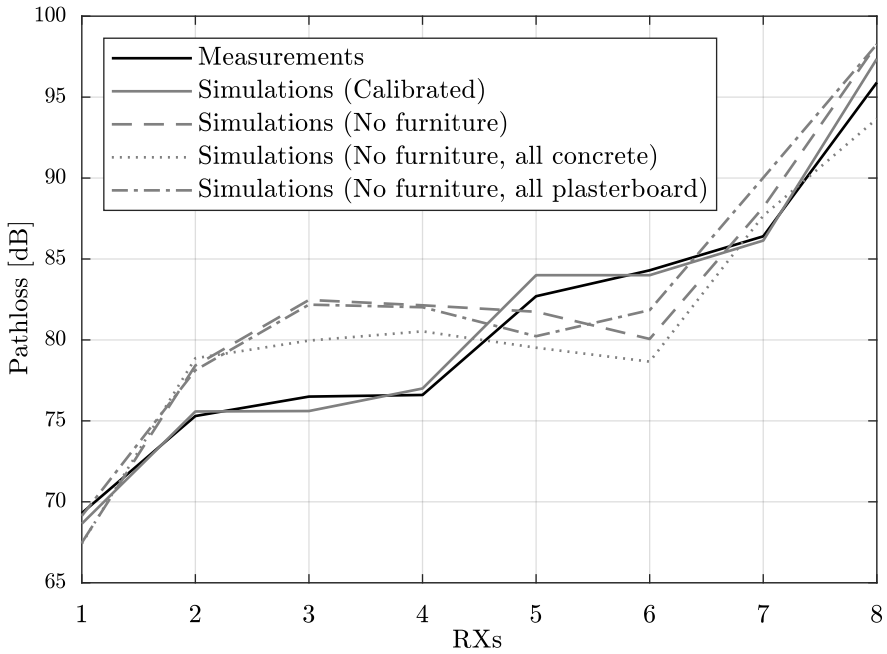

Figure 4.15: Sensitivity analysis.

of 1.9 dB between the measurement and the Configuration 3. However, if we look at the position of RX 5, the difference between the measurements and the calibrated scenario (Configuration 1) values concerning the rest of the

configurations is considerable, being the shortest 2.9 dB. From these results, it could be inferred when the objects and furniture in the scenario have a limited impact (transmission to RX 1) and when they are determinant (transmission to RX 5).

4.5 Conclusions

This chapter has addressed issues related to realistic channel modeling in the mmW band. In this sense, the study has been divided into two main branches: body blockage modeling and the modeling of indoor scenarios. In particular, in Section 4.2, different modifications to the 3GPP body blockage model were proposed and validated with a measurement campaign. These modifications aim to obtain values of body blockage losses at the mmW band that are closer to reality. In addition, the realistic modeling of the scenario and the channel has been deepened, and a simulation tool based on RT techniques has been presented. Finally, the impact of realistic scenario modeling on the channel model itself has been evaluated, concluding that in indoor scenarios at the mmW band, the influence of the scenario furniture and electromagnetic properties of the materials is considerable.

Chapter 5

Precoding optimization in realistic scenarios

In Chapter 2 of this Thesis, different clustering techniques that guarantee the scalability of cell-free massive Multiple-Input Multiple-Output (MIMO) systems and several power allocation options for the downlink case were analyzed. A stochastic channel model and under 6 GHz frequencies were considered for this study for comparison with other state-of-the-art solutions. However, it has been shown in Chapter 4 that the scenario modeling and the objects present in the scenario significantly influence the final results, e.g., on the pathloss. Motivated by this fact, in this chapter, we propose a cell-free massive MIMO deployment in a realistic scenario at millimeter Wave (mmW), specifically in an industrial building. Considering the scenario size and the correspondent network deployment, dividing the network into clusters is unnecessary.

Nevertheless, it would be interesting to analyze the system's performance for different precoding configurations. In this sense, a sum data rate maximization problem is presented subject to different power constraints that correspond to specific demands of the described use case. In the following sections, the basis of precoding optimization in mmW is described, a specific use case is detailed, the optimization solution for the precoders is proposed, the particular scenario is presented, and the achieved results are analyzed.

5.1 Precoding optimization in mmW massive MIMO

The design of precoding schemes plays a fundamental role in mmW massive MIMO communications, where the channel is highly sensitive, and a huge amount of antennas are active simultaneously. By controlling the phases and the amplitudes of the signals, it is possible to guarantee the desired level of service to each User Equipment (UE) in the system based on the flexibility provided by digital techniques.

Optimization algorithms are used to find the suitable precoding coefficients taking into account an objective function that considers the channel and certain constraints that limit the power consumption. Generally, the objective function is the weighted sum rate or the Signal to Interference plus Noise Ratio (SINR), and the power constraints could be sum-power constraints or per-antenna-power constraints.

5.2 Use case

For the deployment of the Fifth Generation (5G) networks in the industry, in addition to ensuring complete coverage, some constraints could arise depending on the characteristics of the scenario and the manufacturing work undertaken. For example, if the production environment is sensitive to radiation, electromagnetic compatibility levels must be assessed to ensure that they do not interfere with the production process. For this reason, creating an Exclusion Volume (EV) in some industrial environments is necessary, where power levels are maintained below a set threshold. In order to guarantee this, in the next section, a precoding optimization problem that considers the power constraints in a specific area of the scenario is presented.

5.3 Precoding design

In order to meet the above use case demands, it is proposed to solve an optimization problem that allows to allocation of power to each antenna so that the total rate is maximized while meeting the received power constraints in the EV. For this purpose, the EV is modeled as a set of reception points. These points are treated in the problem similar to the Receivers (RXs) but considering a more strict power constraint.

The formulation of the problem and its solution have been performed according to [43, 44], applying some minor modifications to consider the power limi-

tation of the EV. In the following, the system model, the modified optimization problem, and the algorithms on which the problem solution is based are detailed.

5.3.1 System model

In this study, a canonical cell-free massive MIMO deployment is considered. The deployment consists of L single-antenna Access Points (APs) distributed in the scenario and K single-antenna receiver points (including U single-antenna receivers and the reception points of the EV). One channel use of the MIMO Broadcast (BC) with an L-antenna transmitter and K single-antenna receiver points (including U single-antenna receivers) is defined by

$$y_k = \mathbf{h}_k^H \mathbf{x} + z_k, k = 1, \ldots, U, \ldots, K. \tag{5.1}$$

where $\mathbf{h}_k, \mathbf{x} \in \mathbb{C}^L$ are the channel vector of receiver point k and the transmitted signal vector, respectively, and $z_k \sim \mathcal{CN}(0, 1)$ is Additive White Gaussian Noise (AWGN). Here, it is assumed that fixed channel vectors are perfectly known to all terminals.

Canonical cell-free massive MIMO could be considered as a special case of the system model described in Section 2.4, where $M = 1$ and $|\mathcal{L}_m| = L$. That being said, (2.8) can be particularized as

$$R_k^{\mathrm{DL}}(\mathbf{Q}_{i_{i=1}}^K) = \log \frac{1 + \mathbf{H}_{k1}^* \mathbf{Q}_k \mathbf{H}_{k1}}{1 + \sum_{i=k+1}^K \mathbf{H}_{k1}^* \mathbf{Q}_i \mathbf{H}_{k1}}, \forall k \leq U. \tag{5.2}$$

The proposed solution aims to fix maximum power levels in the EV based on the design and optimization of the precoders. To do this, we first need to have a set of test points appropriately located in the EV. These points will permit us to know the power reaching the zone.

In order to obtain more realistic results in solving the optimization problem described above, a deterministic channel matrix has been used as input. Then, the elements of the channel matrix obtained from a ray tracing-based simulator have the following form:

$$h_{kl} = \sum_{\alpha=1}^{n} A_\alpha e^{-j\omega_0 \tau_\alpha}, \tag{5.3}$$

where A_α is the amplitude of the α_{th} ray, n is the total number of rays, τ is the time delay of the α_{th} ray, and ω_0 is the carrier frequency.

5.3.2 Optimization problem

In this chapter, it is proposed to maximize the sum data rate subject to different per-antenna power constraints. Mathematically, it can be expressed as follows

$$\begin{aligned} \max_{\{\mathbf{Q}_k\}_{k=1}^{K}} \quad & \sum_{k=1}^{U} R_k(\{\mathbf{Q}_i\}_{i=1}^{U}) \\ \text{s.t.} \quad & \mathbf{Q}_k \succeq 0, \\ & \sum_{k=1}^{K} q_{kl} \leq P_l, \\ & \sum_{k=U+1}^{K} q_{kl} \leq \frac{1}{\rho} P_l, \end{aligned} \tag{5.4}$$

for $l = 1, \ldots, L$ where P_l is the maximum power available at the l-th AP, and ρ is the power limitation coefficient applied to the EV receiver points.

The solution of (5.4) can be computed efficiently by solving a sequence of convex problems.

Based on the BC-Multiple Access Channel (MAC) duality considering per-antenna power constraints [76], the "dual MAC" corresponding to (5.1) as the multiple-access Gaussian channel is defined as

$$\mathbf{y} = \sum_{k=1}^{K} \mathbf{h}_k x_k + \mathbf{z}, \tag{5.5}$$

where $\mathbf{y}, \mathbf{z} \in \mathbb{C}^M, \mathbf{z} \sim \mathcal{CN}(\mathbf{0}, \mathbf{\Sigma}_z(\lambda))$ with $\mathbf{\Sigma}_z(\lambda) = \sum_{l=1}^{L} \lambda_l$ for some vector of non-negative coefficients $\lambda \geq \mathbf{0}$ and each transmitter has power constraint $\mathbb{E}[|x_k|^2] \leq p_k$, subject to total sum-power constraints

$$\sum_{k=1}^{K} p_k \leq \sum_{l=1}^{L} \lambda_l P_l, \tag{5.6}$$

$$\sum_{k=U+1}^{K} p_k \leq \sum_{l=1}^{L} \lambda_l \frac{P_l}{\rho}. \tag{5.7}$$

Then, for any $\lambda \geq \mathbf{0}$, the value of the original MIMO BC sum rate maximization problem is upper-bounded by the value of the new MAC sum rate maximization problem

$$\begin{aligned} \max \quad & \sum_{k=1}^{K} \hat{R}_k \\ \text{s.t.} \quad & \hat{R} \in \mathcal{C}_{MAC} \end{aligned} \tag{5.8}$$

where $\mathcal{C}_{MAC}$ denotes the capacity region of the dual MAC defined above for given parameters λ and $\{P_l\}$ is the non-negative power coefficients.

5.3.3 Solution

The solution of (5.8) is achieved by *successive decoding* in the order $K, K-1, \ldots, 1$, i.e., the reverse of the Dirty Paper Coding (DPC) encoding order. Furthermore, the upper bound provided by the dual MAC is tight: denoting by $g(\lambda)$ the value of the dual-MAC problem for a given λ, the value of the MIMO BC problem can be obtained by minimizing $g(\lambda)$ with respect to $\lambda \geq 0$. Hence, the MIMO BC weighted sum rate maximization problem can be solved by iterating between one "outer problem" solving the minimization of $g(\lambda)$ and an "inner problem" solving (5.8) for fixed λ. An efficient solution of the inner problem is obtained using the *ellipsoid method* while the outer problem is solved using the *subgradient method*. The direct application to a similar problem of this methods is explained in [43, 44] while a more general description is given below.

Subgradient method [77]

Let f be a convex function defined on n-dimensional Euclidean space E_n. The *subgradient method* is an algorithm which generates a sequence $x_k{}_{k=0}^{\infty}$ according to the formula

$$x_{k+1} = x_k - h_{k+1}(x_k) g_f(x_k), \tag{5.9}$$

where x_0 is a given starting point, k is the number of iterations, h_{k+1} is the $k+1$ step size and g_f is any subgradient at x_k. At each iteration, a step is taken in the direction of a negative subgradient. As the new iteration is not necessary the best, the current result should be compared with the former in order to save the best of them, being $f_{best}^k = \min_{j=1,\ldots,k}(f^j)$.

Ellipsoid method [78]

The *ellipsoid method* is an iterative method for determining the feasibility of a system of linear inequalities. With this method, it is possible to find the optimal solution in a number of steps that is polynomial in the input size. Suppose we wish to find an n-vector x satisfying

$$A^T x \leq b \tag{5.10}$$

where A^T is $m \times n$ and b is an m-vector. The columns of A, corresponding to outward normals to the constraints, are denoted $\alpha_1, \alpha_2, \ldots, \alpha_m$, and the

components of β are denoted $\beta_1, \beta_2, \ldots, \beta_m$. Thus (5.10) can be restated as

$$\alpha_i^T x \leq \beta_i, i = 1, 2, \ldots, m. \tag{5.11}$$

We assume throughout that m is greater than one.

The ellipsoid method constructs a sequence of ellipsoids $E_0, E_1, \ldots, E_k, \ldots$, each of which contains a point satisfying (5.10), if one exists. On the $k+1$st iteration, the method checks whether the center x_k of the current ellipsoid E_k satisfies the constraints (5.10). If so, the method stops. If not, some constraint violated by x_k, say

$$\alpha^T x \leq \beta \tag{5.12}$$

is chosen and the ellipsoid of minimum volume that contains the half-ellipsoid

$$x \in E_k | \alpha^T x \leq \alpha^T x_k \tag{5.13}$$

is constructed. This new ellipsoid and its center are denoted by E_{k+1} and x_{k+1}, respectively, and the above iterative step is repeated.

5.4 Presentation of the scenario

A fictitious indoor industrial scenario has been modeled to evaluate the solution. The propagation environment consists of a server hall with several corridors formed by metallic machinery. This environment is characterized by high dispersion, specular and diffuse components that enrich the radio channel. The dimensions of the scenario are 50 m $\times$ 50 m. The scenario height is 5 m. The EV is delimited by a cube of 1 m^3. For more details, see Fig. 5.1.

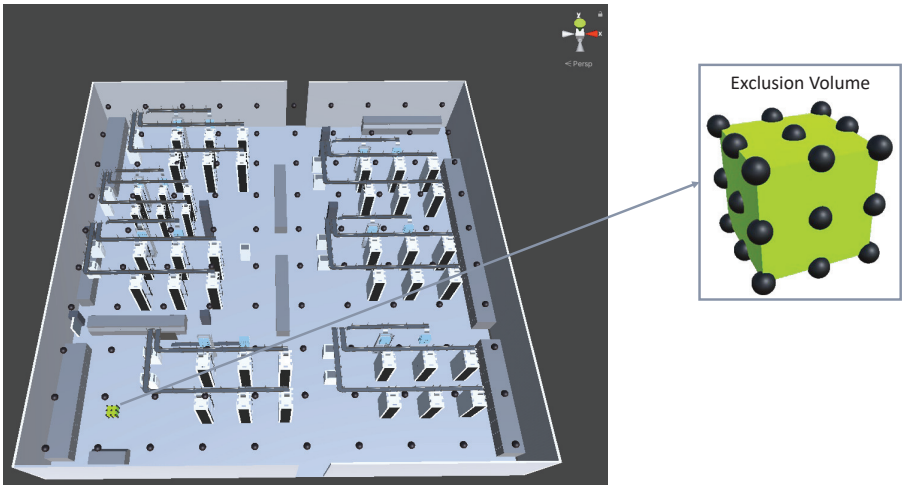

Figure 5.1: Industrial scenario and EV.

The deployment consists of 100 single-antenna APs mounted on the ceiling, uniformly distributed on the scenario with a spacing of 5 m, and connected to a single processing unit, allowing the AP to coordinate APs. Additionally, there are 27 testing points allocated in the EV (represented by a green cube in 5.1).

5.5 Results and analysis

In order to evaluate the proposed solution, the optimization problem has been solved first without taking into account the EV and then taking into account the EV. The values of both maximum received power and maximum achieved data rate has been obtained point by point for a number of intended UE positions, assuming that there is only one UE in the scenario and it is located in the point being measured. The simulation parameters are shown in the table below.

To determine the received power at each point in the scenario, including the EV, three cases have been selected based on the expected UE position: the first, near the lower left corner; the second, in the central area of the scenario; and the third, near the upper right corner.

Figure 5.2 shows the Cumulative Distribution Function (CDF) of the maximum received power in the scenario in general (Fig. 5.2a) and in the EV (Fig. 5.2b) in particular, when no optimization is considered. As it can be seen, the levels of received power in the EV for the three cases are similar to

Table 5.1: Simulation parameters.

Parameter	Value
Number of APs (L)	100
Number of testing points ($K - U$)	27
Number of intended UE positions	2401
Inter-site distance	5 m
Scenario dimensions	50 m x 50 m
AP height	4 m
EV dimensions	1 m x 1 m x 1 m
Frequency	30 GHz
Transmitted power per AP (P_l)	100 mW
Power limitation coefficient for the EV (ρ)	10000

those experimented in the rest of the scenario. These results can be taken as a reference to compare with the ones obtained when the optimization is performed.

Figure 5.3 shows the CDF of the maximum received power in the scenario in general (Fig. 5.3a) and in the EV (Fig. 5.3b) in particular, when optimization is considered. As can be appreciated, the received power values for UE intended positions remained close to the range of the values shown in Fig. 5.2a, while the received power values in the EV dropped drastically compared to those from Fig. 5.2b. Specifically, the difference in received power levels in the EV is, on average, more than 80 dB for all evaluated cases.

According to the results, the purpose of limiting the power in a certain stage volume has been fulfilled. However, it should not be ignored that this volume has been discretized, evaluating the conditions in a set of points only. Therefore, there is a possibility that the conditions may not be fulfilled in other points of the volume different from those evaluated.

Figure 5.4 shows the heatmaps of the maximum achievable data rate in the scenario when no optimization is considered (Fig. 5.4a) and when it is (Fig. 5.4b). As it can be noticed, when optimizing, the maximum achievable data rate decreases around 3 bits/s/Hz, which is not a significant difference.

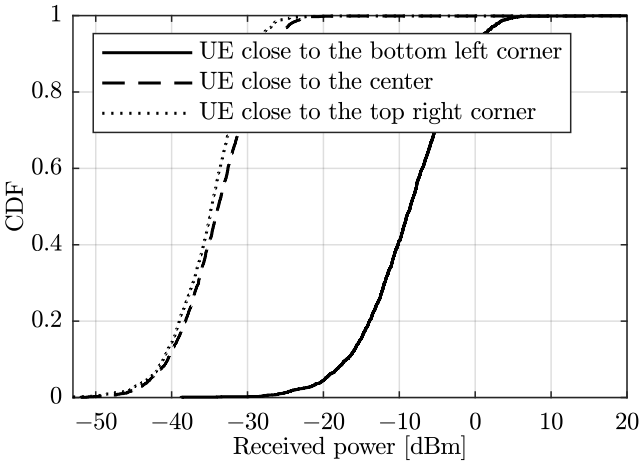

(a) Received power in the scenario considering intended UE positions.

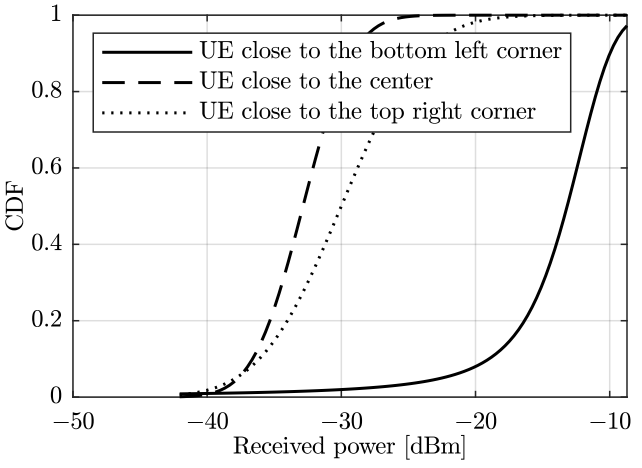

(b) Received power in the EV considering intended UE positions.

Figure 5.2: Maximum received power without considering power constraints for the EV.

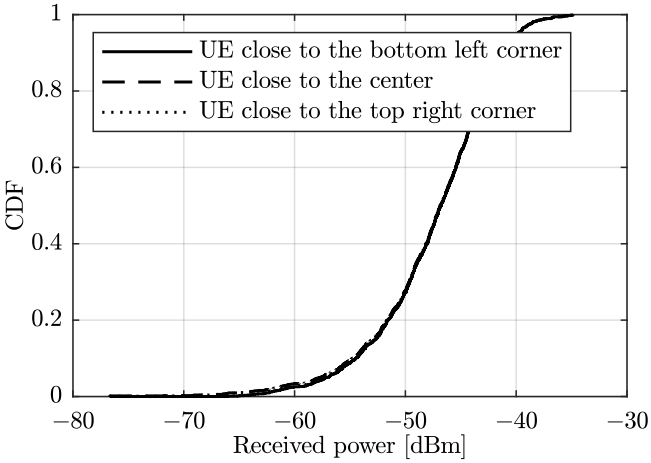

(a) Received power in the scenario considering intended UE positions.

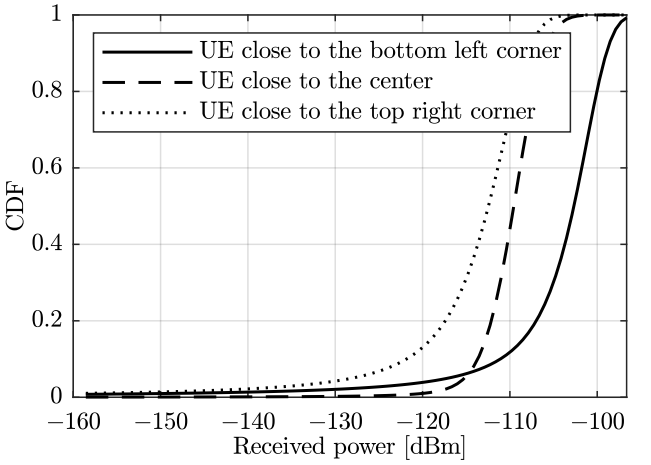

(b) Received power in the EV considering intended UE positions.

Figure 5.3: Maximum received power considering power constraints for the EV.

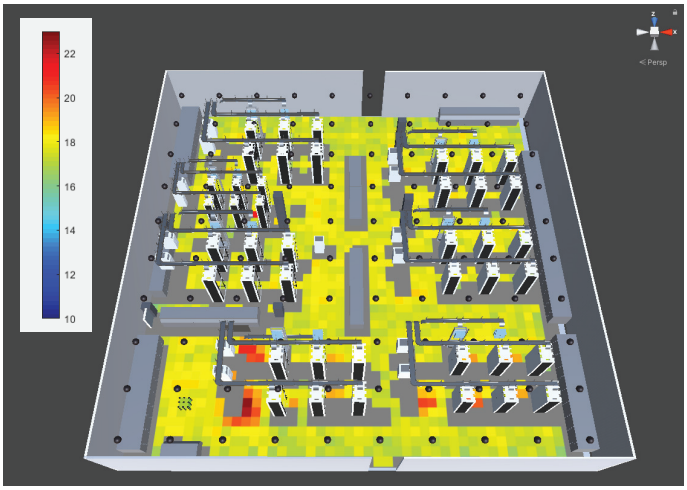

(a) Maximum data rate in bits/s/Hz without considering the EV.

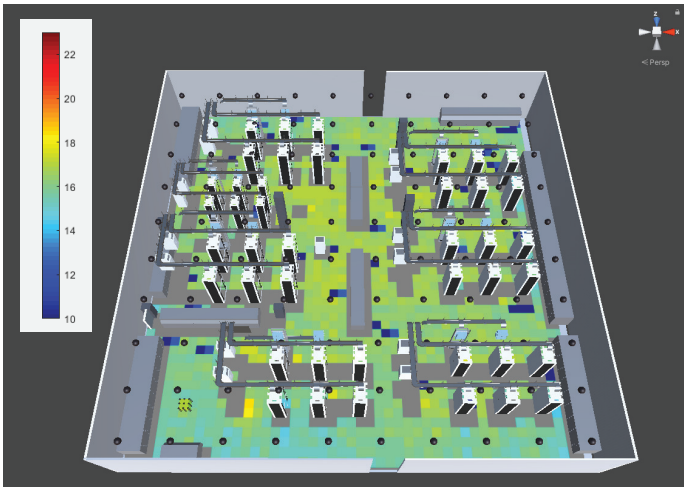

(b) Maximum data rate in bits/s/Hz considering the EV.

Figure 5.4: Maximum data rate considering power constraints for the EV.

5.6 Conclusions

This chapter addresses the problem of electromagnetic isolation of a particular zone of the scenario. First, the scenario and the EV were modeled. Subsequently, a cell-free massive MIMO deployment was proposed for the industrial scenario in focus. Then, the deterministic channel estimation was performed using the ray-tracing-based simulator partially developed in this Thesis. As a final step and for the sake of comparison, the data rate and the received power were calculated with and without considering the power constraints of the EV. It was demonstrated that a good trade-off between the data rate achieved and the power levels in the EV is possible. In particular, for the configuration evaluated in Section 5.4, the power is reduced by around 80 dB while the data rate dreceases around 3 bits/s/Hz only. As it can be intuited, the more restricted the power level in the EV, the lower the data rate level will be obtained.

Chapter 6

Conclusions and future work

6.1 Concluding remarks

This doctoral Thesis addresses three main problems in cell-free massive Multiple-Input Multiple-Output (MIMO): the impact of the network topology, the realistic channel modeling at millimeter Wave (mmW), and the precoding optimization in realistic scenarios.

Related to the first problem, the impact of the network topology, both logical and physical, on performance has been studied. Specifically, the scalability of cell-free massive MIMO systems has been analyzed. This analysis corroborates the idea discussed in other works that cell-free massive MIMO in its canonical form is not scalable. Given this problem, different clustering techniques have been proposed for both uplink and downlink transmission. The main difference between them is how they seek to obtain the best performance: in one case, the user is in the center of the cluster eliminating edge effects, and in the other, the aim is to eliminate or mitigate interference by creating disjoint clusters. By comparing the clustering solutions, it has been seen that the most convenient solution for the uplink case is a combination of the two original solutions, i.e., semi-overlapping clusters with users in positions close to the center. While, for the downlink case, the cluster configuration should facilitate power allocation and, as the results show, the solution with disjoint clusters wins in this case. Concerning the network's physical topology, the characteristics of the front-hauls with dedicated and serial links have been analyzed in the context of the cell-free massive MIMO systems. Likewise, the

power modeling implications of different deployments have been analyzed, and simple modifications to the traditional power consumption models have been proposed to consider the particularities of serial implementations.

Regarding the second problem addressed, the propagation phenomena have been described and how they are affected by the presence of people, objects, furniture, building structures, etc., in a given environment, especially at the mmW band. In this sense, a measurement campaign has been carried out to estimate the pathloss due to human body blockage, and from this, a series of modifications have been applied to the Third Generation Partnership Project (3GPP) human body blockage model. Additionally, an indoor scenario has been realistically modeled in 3D using a channel simulation tool based on ray tracing and developed at the UPV. Subsequently, a sensitivity analysis has been carried out to determine the impact of the 3d model accuracy on pathloss estimation. From this, it is concluded that both the objects present in the scenario and their materials considerably influence the results' accuracy.

Finally, motivated by the specific demands that a realistic scenario may have and the need to respond to them, the design of precoders under certain circumstances has been studied in depth. In particular, a use case has been described. The main requirement of this use case is to ensure that the received power in a certain area of the scenario is below a certain threshold. Faced with this challenge, the corresponding optimization problem has been posed, and a solution has been found. The results corroborate that, relying on the intrinsic flexibility of digital precoders and cell-free massive MIMO deployments, it is possible to guarantee a maximum received power in a certain area of the scenario while maximizing the achievable rate in the rest.

It is necessary to analyze each of the hypotheses formulated in this Thesis and indicate how this research work has answered each of them:

- Hypothesis 1: Cell-free massive MIMO systems are not scalable in their canonical approach. In this sense, the sufficient and necessary criteria to consider when a system is scalable were analyzed. These criteria, as expected, are not met by a canonical systems but by the systems that implement the clustering solutions proposed in this Thesis.

- Hypothesis 2: Power consumption modeling should adapt to the network's physical topology. A study of the power consumption behavior in deployments ranging from fully dedicated front-haul to fully serial front-haul has been carried out. The results of this study highlight the errors in power consumption estimation that could be made if serial deployments continue to be analyzed with the current power consumption model. Motivated by this fact, minor modifications to the power consumption model have been proposed to take into account the power savings obtained when

connecting Access Points (APs) in series, specifically in cell-free massive MIMO deployments.

- Hypothesis 3: Scenario modeling affects channel modeling. A sensitivity study of the channel modeling accuracy to the level of realistic 3D modeling in the mmW band was carried out to corroborate this hypothesis. This study confirmed the influence of any object or structure in the scene on the radio channel obtained. Likewise, the materials present in the scenery have proven to play a determining role.

- Hypothesis 4: The optimal precoders will depend on the accuracy of the scenario and channel modeling. A specific use case has been analyzed in this sense, modeling the corresponding optimization problem and finding its solution. The mathematical modeling of the optimization problem shows the high dependence of its resolution on the channel between each AP and each User Equipment (UE), generally assigning more power to those with a better channel as long as the constraints are respected.

6.2 Future research lines

This Thesis is no more than the starting point for many other research topics. In particular, the following aspects can be highlighted:

- A broader study of clustering solutions in both uplink and downlink should be made, making clear the implications of such solutions at both the physical and signal processing levels.

- The modeling of the fixed front-haul power as a function of the front-haul technology should be studied. In addition, sequential uplink processing implications over uplink power consumption should be analyzed.

- The sensitivity study of realistic modeling should be extended, considering situations where propagation phenomena such as diffraction or transmission have a more significant impact.

- Regarding the design of precoders, the problems to be solved can be as varied as life itself. Focusing on the use case study, it would be helpful to determine the channel estimation frequency and, consequently, the maximum time available for calculating precoders to achieve and maintain a given performance. This way, it would be possible to design new algorithms for calculating precoders, considering the time constraint.

References

[1] Radiocommunication Sector of ITU, "IMT Vision – Framework and overall objectives of the future development of IMT for 2020 and beyond," International Telecommunication Union, M 2083-0, Sep. 2015.

[2] Wireless Communication and Networking Laboratory, "Protocols, adaptation, and spectrum allocation for 5G millimeter-wave systems motivation," https://wireless.ece.arizona.edu.

[3] T. L. Marzetta, "Noncooperative cellular wireless with unlimited numbers of base station antennas," *IEEE Transactions on Wireless Communications*, vol. 9, no. 11, pp. 3590–3600, Nov. 2010.

[4] E. Bjornson, L. V. der Perre, S. Buzzi, and E. G. Larsson, "Massive MIMO in sub-6 GHz and mmWave: Physical, practical, and use-case differences," *IEEE Wireless Communications*, vol. 26, no. 2, pp. 100–108, Apr. 2019.

[5] C.-X. Wang, F. Haider, X. Gao, X.-H. You, Y. Yang, D. Yuan, H. Aggoune, H. Haas, S. Fletcher, and E. Hepsaydir, "Cellular architecture and key technologies for 5G wireless communication networks," *IEEE Communications Magazine*, vol. 52, no. 2, pp. 122–130, Feb. 2014.

[6] A. Osseiran, J. F. Monserrat, and W. Mohr, *Coordinated MultiPoint (CoMP) Systems.* Wiley, 2011, pp. 121–155.

[7] H. Q. Ngo, A. Ashikhmin, H. Yang, E. G. Larsson, and T. L. Marzetta, "Cell-free massive MIMO versus small cells," *IEEE Transactions on Wireless Communications*, vol. 16, no. 3, pp. 1834–1850, Mar. 2017.

[8] S. Buzzi and C. D'Andrea, "Cell-free massive MIMO: User-centric approach," *IEEE Wireless Communications Letters*, vol. 6, no. 6, pp. 706–709, Dec. 2017.

[9] M. Alonzo and S. Buzzi, "Cell-free and user-centric massive MIMO at millimeter wave frequencies," in *2017 IEEE 28th Annual International Symposium on Personal, Indoor, and Mobile Radio Communications (PIMRC)*. IEEE, Oct. 2017.

[10] S. A. Busari, K. M. S. Huq, S. Mumtaz, L. Dai, and J. Rodriguez, "Millimeter-wave massive MIMO communication for future wireless systems: A survey," *IEEE Communications Surveys & Tutorials*, vol. 20, no. 2, pp. 836 – 869, May 2018.

[11] S. Gimenez, S. Roger, P. Baracca, D. Martín-Sacristán, J. F. Monserrat, V. Braun, and H. Halbauer, "Performance evaluation of analog beamforming with hardware impairments for mmW massive MIMO communication in an urban scenario," *Sensors*, vol. 16, no. 10, Sep. 2016. [Online]. Available: https://www.mdpi.com/1424-8220/16/10/1555

[12] M.-T. Martinez-Ingles, J.-V. Rodriguez, J. Pascual-Garcia, J.-M. Molina-Garcia-Pardo, and L. Juan-Llacer, "On the influence of diffuse scattering on multiple-plateau diffraction analysis at mm-Wave frequencies," *IEEE Transactions on Antennas and Propagation*, vol. 67, no. 4, pp. 2130–2135, Apr. 2019.

[13] K. Zarifi, H. Baligh, J. Ma, M. Salem, and A. Maaref, "Radio access virtualization: Cell follows user," in *2014 IEEE 25th Annual International Symposium on Personal, Indoor, and Mobile Radio Communication (PIMRC)*. IEEE, Sep. 2014.

[14] G. Interdonato, P. Frenger, and E. G. Larsson, "Scalability aspects of cell-free massive MIMO," in *ICC 2019 - 2019 IEEE International Conference on Communications (ICC)*. IEEE, May 2019.

[15] G. Interdonato, E. Björnson, H. Q. Ngo, P. Frenger, and E. G. Larsson, "Ubiquitous cell-free massive MIMO communications," *EURASIP Journal on Wireless Communications and Networking*, vol. 2019, no. 1, Aug. 2019.

[16] Z. H. Shaik, E. Björnson, and E. G. Larsson, "Cell-free massive mimo with radio stripes and sequential uplink processing," in *2020 IEEE International Conference on Communications Workshops (ICC Workshops)*. IEEE, Jun. 2020, pp. 1–6.

[17] E. Nayebi, A. Ashikhmin, T. L. Marzetta, H. Yang, and B. D. Rao, "Precoding and power optimization in cell-free massive MIMO systems," *IEEE Transactions on Wireless Communications*, vol. 16, no. 7, pp. 4445–4459, Jul. 2017.

[18] L. D. Nguyen, T. Q. Duong, H. Q. Ngo, and K. Tourki, "Energy efficiency in cell-free massive MIMO with zero-forcing precoding design," *IEEE Communications Letters*, vol. 21, no. 8, pp. 1871–1874, Aug. 2017.

[19] G. Interdonato, M. Karlsson, E. Bjornson, and E. G. Larsson, "Local partial zero-forcing precoding for cell-free massive MIMO," *IEEE Transactions on Wireless Communications*, vol. 19, no. 7, pp. 4758–4774, Jul. 2020.

[20] T. C. Mai, H. Q. Ngo, M. Egan, and T. Q. Duong, "Pilot power control for cell-free massive MIMO," *IEEE Transactions on Vehicular Technology*, vol. 67, no. 11, pp. 11 264–11 268, Nov. 2018.

[21] M. Bashar, K. Cumanan, A. G. Burr, M. Debbah, and H. Q. Ngo, "On the uplink max–min SINR of cell-free massive MIMO systems," *IEEE Transactions on Wireless Communications*, vol. 18, no. 4, pp. 2021–2036, Apr. 2019.

[22] M. Alonzo, S. Buzzi, A. Zappone, and C. D'Elia, "Energy-efficient power control in cell-free and user-centric massive MIMO at millimeter wave," *IEEE Transactions on Green Communications and Networking*, vol. 3, no. 3, pp. 651–663, Sep. 2019.

[23] J. Garcia-Morales, G. Femenias, and F. Riera-Palou, "Energy-efficient access-point sleep-mode techniques for cell-free mmWave massive MIMO networks with non-uniform spatial traffic density," *IEEE Access*, vol. 8, pp. 137 587–137 605, Jul. 2020.

[24] ETSI, "5G; study on channel model for frequencies from 0.5 to 100 ghz (3gpp tr 38.901 version 16.1.0 release 16)," 3GPP, Tech. Rep., 2020.

[25] METIS2020, "METIS channel model," METIS2020, Tech. Rep., Deliverable D1.4 v3, July 2015. [Online]. Available: https://www.metis2020.com/wp-content/uploads/deliverables/METIS_D1.4v1.0.pdf

[26] K. Haneda, S. Nguyen, A. Karttunen, J. Järveläinen, A. Bamba, R. D'Errico, J. Medbo, F. Undi, S. Jaeckel, N. Iqbal, J. Luo, M. Rybakowski, C. Diakhate, J.-M. Conrat, A. Naehring, S. Wu, A. Goulianos, E. Mellios, and M. Peter, "Measurement results and final mmMAGIC channel models," May 2017.

[27] S. Sun, G. R. MacCartney, and T. S. Rappaport, "A novel millimeter-wave channel simulator and applications for 5G wireless communications," in *2017 IEEE International Conference on Communications (ICC)*. IEEE, May 2017.

[28] S. Jaeckel, L. Raschkowski, K. Borner, and L. Thiele, "QuaDRiGa: A 3-D multi-cell channel model with time evolution for enabling virtual field trials," *IEEE Transactions on Antennas and Propagation*, vol. 62, no. 6, pp. 3242–3256, Jun. 2014.

[29] IEEE, "IEEE standard for information technology–telecommunications and information exchange between systems - local and metropolitan area networks–specific requirements - part 11: Wireless LAN medium access control (MAC) and physical layer (PHY) specifications," *IEEE Std 802.11-2020 (Revision of IEEE Std 802.11-2016)*, pp. 1–4379, 2021.

[30] R. J. Weiler, M. Peter, W. Keusgen, A. Maltsev, I. Karls, A. Pudeyev, I. Bolotin, I. Siaud, and A.-M. Ulmer-Moll, "Quasi-deterministic millimeter-wave channel models in MiWEBA," *EURASIP Journal on Wireless Communications and Networking*, vol. 2016, no. 1, Mar. 2016.

[31] E. G. Larsson and L. V. der Perre, "Massive MIMO for 5G," *IEEE 5G Tech Focus*, vol. 1, no. 1, Mar. 2017.

[32] N. Tawa, T. Kuwabara, Y. Maruta, M. Tanio, and T. Kaneko, "28 GHz downlink multi-user mimo experimental verification using 360 element digital AAS for 5G massive MIMO," in *Proceedings of the 48th European Microwave Conference*, Sep. 2018.

[33] T. Lo, "Maximum ratio transmission," *IEEE Transactions on Communications*, vol. 47, no. 10, pp. 1458–1461, Oct. 1999.

[34] R. W. Lucky, "Automatic equalization for digital communication," *The Bell System Technical Journal*, vol. 44, no. 4, pp. 547–588, Apr. 1965.

[35] D. Calabuig, R. H. Gohary, and H. Yanikomeroglu, "Optimum transmission through the multiple-antenna Gaussian multiple access channel," *IEEE Transactions on Information Theory*, vol. 62, no. 1, pp. 230–243, Jan. 2016.

[36] H. Q. Ngo, *Cell-Free Massive MIMO*. Cham: Springer International Publishing, 2020, pp. 165–169. [Online]. Available: https://doi.org/10.1007/978-3-319-78262-1_137

[37] E. Tanghe, W. Joseph, L. Verloock, L. Martens, H. Capoen, K. Herwegen, and W. Vantomme, "The industrial indoor channel: large-scale and temporal fading at 900, 2400, and 5200 MHz," *IEEE Transactions on Wireless Communications*, vol. 7, no. 7, pp. 2740–2751, Jul. 2008.

[38] Radiocommunication Sector of ITU, "Guidelines for evaluation of radio interface technologies for IMT-Advanced," no. 2135-1, Dec. 2009.

[39] E. Björnson and L. Sanguinetti, "Scalable cell-free massive MIMO systems," *IEEE Transactions on Communications*, vol. 68, no. 7, pp. 4247–4261, Jul. 2020.

[40] S. Verdu *et al.*, *Multiuser detection*. Cambridge university press, 1998.

[41] M. Costa, "Writing on dirty paper (corresp.)," *IEEE Transactions on Information Theory*, vol. 29, no. 3, pp. 439–441, May 1983.

[42] S. Vishwanath, N. Jindal, and A. Goldsmith, "Duality, achievable rates, and sum-rate capacity of Gaussian MIMO broadcast channels," *IEEE Transactions on Information Theory*, vol. 49, no. 10, pp. 2658–2668, Oct. 2003.

[43] H. Huh, H. Papadopoulos, and G. Caire, "MIMO broadcast channel optimization under general linear constraints," in *2009 IEEE International Symposium on Information Theory*, Jun. 2009, pp. 2664–2668.

[44] L. Zhang, R. Zhang, Y.-C. Liang, Y. Xin, and H. V. Poor, "On Gaussian MIMO BC-MAC duality with multiple transmit covariance constraints," *IEEE Transactions on Information Theory*, vol. 58, no. 4, pp. 2064–2078, Apr. 2012.

[45] W. Yu, "Uplink-downlink duality via minimax duality," *IEEE Transactions on Information Theory*, vol. 52, no. 2, pp. 361–374, Feb. 2006.

[46] H. Q. Ngo, L.-N. Tran, T. Q. Duong, M. Matthaiou, and E. G. Larsson, "On the total energy efficiency of cell-free massive MIMO," *IEEE Transactions on Green Communications and Networking*, vol. 2, no. 1, pp. 25–39, Mar. 2018.

[47] Ericsson, URL https://www.ericsson.com/en/blog/2019/2/radio-stripes, 2020.

[48] A. Papazafeiropoulos, H. Q. Ngo, P. Kourtessis, S. Chatzinotas, and J. M. Senior, "Towards optimal energy efficiency in cell-free massive MIMO systems," *IEEE Transactions on Green Communications and Networking*, vol. 5, no. 2, pp. 816–831, Jun. 2021.

[49] E. Bjornson, L. Sanguinetti, and M. Kountouris, "Deploying dense networks for maximal energy efficiency: Small cells meet massive MIMO," *IEEE Journal on Selected Areas in Communications*, vol. 34, no. 4, pp. 832–847, Apr. 2016.

[50] B. Dai and W. Yu, "Energy efficiency of downlink transmission strategies for cloud radio access networks," *IEEE Journal on Selected Areas in Communications*, vol. 34, no. 4, pp. 1037–1050, Apr. 2016.

[51] A. J. Fehske, P. Marsch, and G. P. Fettweis, "Bit per Joule efficiency of cooperating base stations in cellular networks," in *2010 IEEE Globecom workshops*. IEEE, Dec. 2010, pp. 1406–1411.

[52] J. Hederen and P. Frenger, "Improved antenna arrangement for distributed massive MIMO," Dec. 17 2020, US Patent App. 16/764,126.

[53] S. A. Inca, "Serious game engineering and lighting models for the realistic emulation of 5G systems," Ph.D. dissertation, Universitat Politècnica de València, 2019.

[54] M. Jacob, S. Priebe, T. Kürner, M. Peter, M. Wisotzki, R. Felbecker, and W. Keusgen, "Extension and validation of the IEEE 802.11ad 60 GHz human blockage model," in *2013 7th European Conference on Antennas and Propagation (EuCAP)*, Apr. 2013, pp. 2806–2810.

[55] ETSI, "5G; Study on channel model for frequencies from 0.5 to 100 GHz (3GPP TR 38.901 version 14.0.0 Release 14)," 3GPP, Tech. Rep., 2017.

[56] M. Nakamura, M. Sasaki, N. Kita, and Y. Takatori, "Path loss model in crowded areas considering multiple human blockage at 4.7 and 26.4 GHz," in *2017 IEEE Conference on Antenna Measurements & Applications (CAMA)*. IEEE, Dec. 2017.

[57] G. R. MacCartney, S. Deng, S. Sun, and T. S. Rappaport, "Millimeter-wave human blockage at 73 GHz with a simple double knife-edge diffraction model and extension for directional antennas," in *2016 IEEE 84th Vehicular Technology Conference (VTC-Fall)*. IEEE, Sep. 2016.

[58] D. Prado-Alvarez, S. Inca, D. Martín-Sacristán, and J. F. Monserrat, "Millimeter-wave human blockage model enhancements for directional antennas and multiple blockers," *IEEE Communications Letters*, vol. 25, no. 9, pp. 2776–2780, Sep. 2021.

[59] D. Moltchanov, A. Ometov, S. Andreev, and Y. Koucheryavy, "Upper bound on capacity of 5G mmWave cellular with multi-connectivity capabilities," *Electronics Letters*, vol. 54, no. 11, pp. 724–726, May 2018.

[60] U. T. Virk and K. Haneda, "Modeling human blockage at 5G millimeter-wave frequencies," *IEEE Transactions on Antennas and Propagation*, vol. 68, no. 3, pp. 2256–2266, Mar. 2020.

[61] Steatite, "Wideband Horn Antenna 18 to 40 GHz WRD180," Datasheet, 2019.

[62] P. Kyösti, J. Meinilä, L. Hentila, X. Zhao, T. Jämsä, C. Schneider, M. Narandzic, M. Milojević, A. Hong, J. Ylitalo, V.-M. Holappa, M. Alatossava, R. Bultitude, Y. Jong, and T. Rautiainen, "WINNER II channel models," Tech. Rep., Feb. 2008.

[63] 3GPP TSG RAN, "Study on 3D channel model for LTE (Release 12)," 3GPP, TR 36.873 v12.7.0, Dec. 2017.

[64] CloudRT, url: http://www.raytracer.cloud, 2019.

[65] Altair WinProp, url:https://altairhyperworks.com, 2019.

[66] RENCOM, url:https://www.remcom.com, 2019.

[67] Ranplan Wireless, url: https://ranplanwireless.com, 2019.

[68] SIDAREL, url: https://www.siradel.com, 2019.

[69] Unity 3D, url: https://unity.com, 2019.

[70] A. Navarro, D. Guevara, and N. Cardona, "Game engines ray-tracing models for indoor channel modeling," in *IEEE Antennas and Propagation Society International Symposium (APSURSI)*, Jul. 2014.

[71] D. Garcia-Roger, D. Martín-Sacristán, S. Roger, J. F. Monserrat, A. Kousaridas, P. Spapis, S. Ayaz, and C. Zhou, "5G multi-antenna V2V channel modeling with a 3D game engine," in *IEEE Wireless Communications and Networking Conference Workshops (WCNCW): Centimetre and Millimetre Wave based communications for 5G Networks (CmMmW5G)*, Apr. 2018.

[72] S. Inca, D. Prado-Alvarez, D. Martín-Sacristán, and J. F. Monserrat, "Channel modelling based on game engines light physics for mmW in indoor scenarios," in *2020 14th European Conference on Antennas and Propagation (EuCAP)*, Mar. 2020, pp. 1–5.

[73] G. Liang and H. L. Bertoni, "A new approach to 3-D ray tracing for propagation prediction in cities," *IEEE Transactions on Antennas and Propagation*, vol. 46, no. 6, pp. 853–863, Jun. 1998.

[74] ITU-R, "Effects of building materials and structures on radiowave propagation above about 100 MHz ," ITU, TR P. 204010, Oct. 2015.

[75] G. R. Maccartney, T. S. Rappaport, S. Sun, and S. Deng, "Indoor office wideband millimeter-wave propagation measurements and channel models at 28 and 73 GHz for ultra-dense 5G wireless networks," *IEEE Access*, vol. 3, pp. 2388–2424, Oct. 2015.

[76] W. Yu and T. Lan, "Transmitter optimization for the multi-antenna downlink with per-antenna power constraints," *IEEE Transactions on Signal Processing*, vol. 55, no. 6, pp. 2646–2660, Jun. 2007.

[77] N. Z. Shor, *Minimization methods for non-differentiable functions*. Springer Science & Business Media, 2012, vol. 3.

[78] R. G. Bland, D. Goldfarb, and M. J. Todd, "The ellipsoid method: A survey," *Operations research*, vol. 29, no. 6, pp. 1039–1091, Dec. 1981.